UNIVERSITY OF COPENHAGEN
FACULTY OF SCIENCE

Master's thesis

Molecular Gas in a Massive Main-sequence Galaxy at z = 3

Han Lei

Supervisors: Georgios Magdis, Francesco Valentino

Submitted: July 29, 2022

Abstract

Since molecular hydrogen is the fuel of star formation, the reservoir of molecular hydrogen mass is the key to understand the star formation processes in galaxies and the galaxy evolution across cosmic time. The traditional gas mass tracer is carbon monoxide. Its line luminosity can be converted into molecular gas mass with a conversion factor. With the observational difficulty at higher redshift and the dependence of conversion factor on various conditions, other tracers should also receive attention. The neutral atomic carbon is an alternative due to its multiple advantages to carbon monoxide.

As a typical main-sequence star-forming galaxy at $z \approx 3$, the study of D49 can hopefully provide knowledge of the Cosmic Noon and the main-sequence at a higher redshift. With the new observations and measurements on D49, its spectral energy distribution is fitted with a novel algorithm `Stardust`. The result is consistent with previous study and does not support a strong active galactic nucleus existing in D49.

A high CO(7-6)-to-IR ratio is found in D49, indicating there are more CO emissions than those from star formation activities. Such high ratios are also found in local galaxy NGC 6240 and distant galaxy BX610 at $z \approx 2$, in both of which the CO emissions are believed to be enhanced by shocks. The similar scenario can possibly exist in D49.

With new detections of [CI] lines, molecular gas mass in D49 can be estimated from their line ratio and line luminosities. In addition to the gas mass estimation from `Stardust` fitting, seven estimates of $M_{\mathrm{H_2}}$ in D49 have been derived. They are consistent within a factor of three or less.

Acknowledgements

When I boarded the plane from Shanghai to Copenhagen in 2020 summer, I could never have imagined that these two years would be so exciting for me. It would be like a river entering a whole new mountain range, and the pictures of a new world would unfold in an orderly manner before my eyes. It is the river's destiny to meander, and that is the very reason to explore the colourful landscape of its banks. Now I am about to finish my journey through a magnificent mountain range and head off to the next unknown terrain.

At this special point, firstly, I would like to express my gratitude to my supervisors, Francesco Valentino and Georgios Magdis, who have been leading me through the valley of distant galaxies and its evolution across cosmic time, paying great patience to my fancy questions, never-ending problems and frequent discussions. Moreover, I have also benefited a lot from the advice and help they have given me as teachers and friends for the next stage of my life at this particular time. I would like to wish them happiness, good health and a successful career.

I also want to say thanks to my mom, my boyfriend Tianyi, my friends Alexandra, Jasper, Bodil, Malthe, Jiaming and Guozhen, those Internet friends who play online games with me, and the cat and dog who I am going to keep in the future. They are an important part of my pleasant life outside of my studies, the warm fireplace for the long Nordic winter nights, twilight and music, the light of the lake in the spring, and the other side of the bank of my life river.

Finally, I want to thank former Spanish soccer player Iker Casillas, who gives me the shimmering light to walk through the fog, the courage to keep fighting, and the faith never to give up.

Contents

Chapter 1

Introduction

1.1 Molecular gas in distant galaxies

Star formation plays an essential role in the evolution of galaxies. It converts gas into stars and, with the death of massive stars, gas and dust will be ejected back into the interstellar medium (ISM). Molecular gas, the fuel for star formation, is therefore the key to understand the star formation processes in galaxies and the galaxy evolution across cosmic time.

Molecular hydrogen, H_2, is the dominating component in molecular gas in galaxies. However, its lack of a permanent dipole moment makes the emission from molecular hydrogen difficult to observe. Its lower roto-vibrational transitions are forbidden, and the first quadropole line lies 500 K above its ground state, which is significantly higher than the temperatures in giant molecular clouds (typically $\sim 10\,\mathrm{K}$). Therefore, reliable tracer molecules are needed to detect molecular gas mass in galaxies.

One of the traditional choices of tracer is carbon monoxide, CO, which is the most abundant molecule after H_2. Its first rotational transition $J = 1 \rightarrow 0$ requires a temperature of $\sim 5\,\mathrm{K}$ and critical density of $2.1 \times 10^3\,\mathrm{cm}^{-3}$, which can be easily excited in molecular clouds, and its wavelength $\lambda_{\mathrm{rest}} = 2.6\,\mathrm{mm}$ ($\nu_{\mathrm{rest}} = 115.27\,\mathrm{GHz}$) falls in a fairly transparent window of atmosphere when it comes from nearby galaxies, making it easy to observe from ground-based telescope. Commonly, there are two ways to express line luminosities at high redshift ([1]):

$$L'_{\mathrm{line}}[\mathrm{K\,km\,s^{-1}\,pc^2}] = 3.25 \times 10^7 S_{\mathrm{line}}\Delta v\, \nu_{\mathrm{obs}}^{-2} D_L^2 (1+z)^{-3}, \tag{1.1}$$

$$L_{\mathrm{line}}[L_\odot] = 1.04 \times 10^{-3} S_{\mathrm{line}}\Delta v D_{\mathrm{L}}^2 \nu_{\mathrm{obs}}, \tag{1.2}$$

where $S_{\mathrm{line}}\Delta v$ is the velocity-integrated line flux in $\mathrm{Jy\,km\,s^{-1}}$, D_L is the luminosity distance in Mpc and ν_{obs} is the observed frequency of the emission line in GHz. The

molecular gas mass can be converted from the CO($J = 1 \rightarrow 0$), hereafter denoted as CO(1-0), with a conversion factor $\alpha_{\rm CO}$ by

$$M_{\rm H_2}[M_\odot] = \alpha_{\rm CO} L'_{\rm CO}. \tag{1.3}$$

Within our Milky Way and Local Group (excluding the Small Magallenic Cloud), the $\alpha_{\rm CO}$ is well-calibrated in a narrow range $\alpha_{\rm CO} = 3 - 6\, M_\odot\,({\rm K\,km\,s^{-1}})^{-1}\,{\rm pc^{-2}}$ ([2]). Its dependence on metallicity, gas surface density and galaxy types is also found ([2, 3]), which brings uncertainty to the estimatation of molecular gas mass.

In addition to the conversion factor issue, CO(1-0) becomes more difficult to observe for galaxies at higher redshifts, and other tracers should also be considered. An alternative is the neutral atomic carbon, [CI]. Its atomic fine structure lines, [CI]($^3{\rm P}_1 - ^3{\rm P}_0$)($\nu_{\rm rest} = 492.16\,{\rm GHz}$) and [CI]($^3{\rm P}_2 - ^3{\rm P}_1$) ($\nu_{\rm rest} = 809.34\,{\rm GHz}$), hereafter denoted as [CI](1-0) and [CI](2-1) respectively, are found to serve as potentially even better tracer than the traditional CO ([4, 5, 6, 7]). Figure 1.1 shows the correlation between $L'_{\rm [CI](1-0)}$ (or $L'_{\rm [CI](1-0)}/L_{\rm IR}$) and $L_{\rm IR}$, which is similar to what is found for CO(1-0), suggesting that [CI] can be an effective tracer. Figure 1.2 shows how CO and [CI] can trace $M_{\rm H_2}$. [CI] lines can be more luminous under various conditions than CO.

In classical model, the [CI] emission comes from the surface of photodissociation region (PDR), where CO is dissociated by UV radiation from O and B stars ([8]). Although its usefulness of being a molecular gas tracer has been questioned, modern 3D PDR models, including turbulence ([9, 10]), nonequilibrium chemistry ([11]), clumpy geometries ([12]), and cosmic rays ([13, 14, 15, 16]), have suggested that [CI] co-exists with CO over a wide range of conditions, with a constant ratio $N([{\rm CI}])/N({\rm CO}) \sim 0.1 - 0.2$ (e.g. [17, 18, 19]). These [CI] lines are generally optically thin in various astrophysical conditions so that we can detect higher column densities of cold molecular gas than CO. The excitation temperatures are 23.6 K and 62.5 K, respectively, and the critical density for collisions with hydrogen atoms is $n_{\rm crit} \approx 10^3\,{\rm cm^{-3}}$. Thus they are able to probe a wide range of ISM. Models show that [CI](1-0) luminosity can correlate with total gas mass $M_{\rm gas}$ better than CO(1-0) ([20]). For high-redshift galaxies, high cosmic-ray rates are expected and thus CO is destroyed, while [CI] can become more abundant ([5, 14, 15, 16]). In addition, the excitation conditions of molecular gas can be directly derived from the line ratio $L'_{\rm [CI](2-1)}/L'_{[CI](1-0)}$, due to its simple three-level structure ([21]).

Under the assumptions of local thermodynamic equilibrium (LTE) and both [CI] lines being optically thin, the neutral atomic carbon mass can be derived from $L'_{\rm [CI](1-0)}$

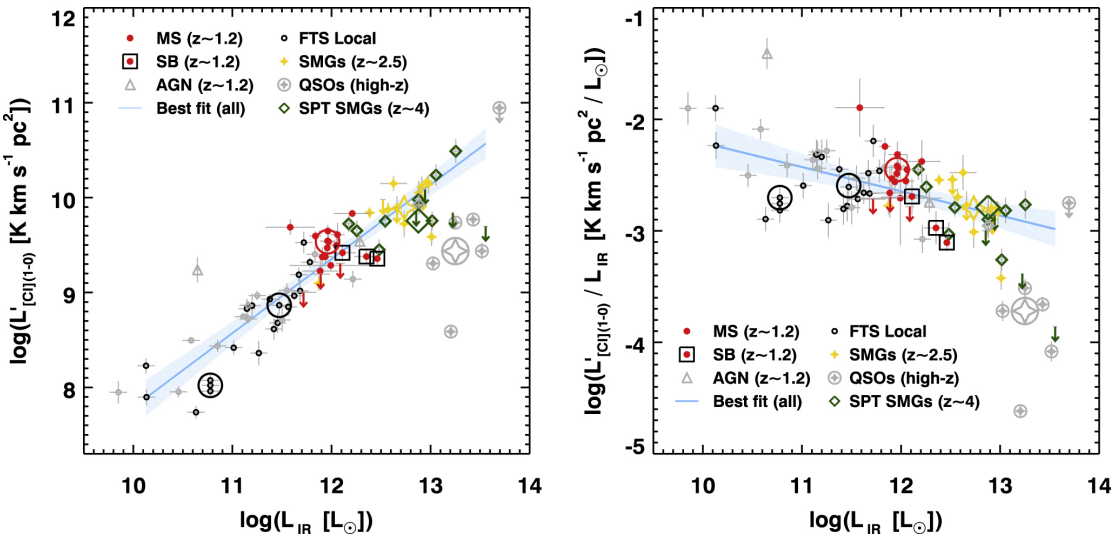

Figure 1.1: *Left:* The $L_{\rm IR}$-$L'_{\rm [CI](1-0)}$ correlation. Samples include $z \sim 1.2$ main-sequence galaxies (red circle), starburst galaxies (black squares), active galactic nuclei (grey triangles), and sub-millimeter galaxies at $z \sim 2.5$ (yellow stars) and at $z \sim 4$ (open green diamonds), in addition to high-redshift quasars (grey stars in open circles). The blue solid line and the filled area represent the best-fit linear correlation and the 95% confidence interval. *Right:* The relation between [CI](1-0)/IR ratio and $L_{\rm IR}$, which is a proxy for the gas depletion timescale vs. SFR. Figures are from [6]

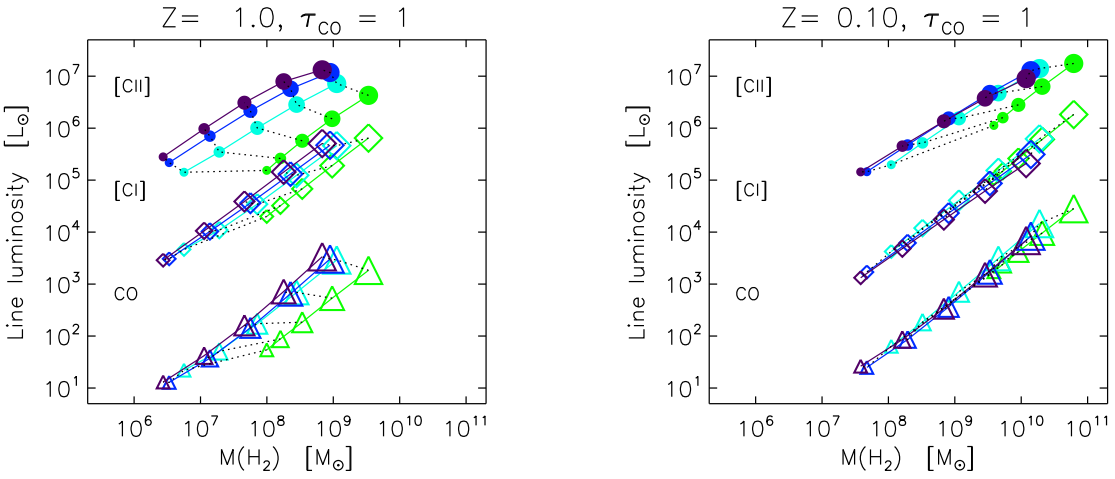

Figure 1.2: *Left:* The relation between molecular gas mass and line luminosities of CO, [CI] and [CII], obtained from models for various densities (labelled by color) and radiation field (labelled by size of marker), for $Z = Z_\odot$ (*left*) and $Z = 0.1Z_\odot$ (*right*). Figures are from [20]

by ([22])

$$M_{\rm [CI]}[M_\odot] = 5.706 \times 10^{-4} Q(T_{\rm ex}) \frac{1}{3} {\rm e}^{23.6/T_{\rm ex}} L'_{\rm [CI](1-0)}, \tag{1.4}$$

where $T_{\rm ex}[{\rm K}] = 38.8 \times \left[\ln\left(2.11 \frac{L'_{\rm [CI](1-0)}}{L'_{\rm [CI](2-1)}}\right)\right]^{-1}$ is the [CI] excitation temperature and $Q(T_{\rm ex}) = 1 + 3{\rm e}^{-23.6/T_{\rm ex}} + 5{\rm e}^{-62.5/T_{\rm ex}}$ is the partition function. Then the neutral atomic carbon mass $M_{\rm [CI]}$ can be converted into $M_{\rm H_2}$ with applying its abundance $X_{\rm [CI]} = {\rm [CI]}/{\rm [H_2]} = M_{\rm [CI]}/(6M_{\rm H_2})$. Furthermore, the combination of CO and [CI] emissions is able to reveal the density and temperature of molecular gas by applying the Large Velocity Gradient (LVG) model([23]). Such a method has been successfully applied to study the ISM condition in galaxies at $z \sim 2$ (e.g. [24, 25]).

1.2 D49 as a template main-sequence galaxy at Cosmic Noon

A peak of star formation rate density (SFRD) is found at $z \sim 2-3$ (e.g. [26, 27], Figure 1.3), indicating that frequent star-forming activity is occurring during this period of the Universe. Such a period is recently known as Cosmic Noon. It makes those galaxies at $z \sim 2-3$ important to understand the evolution of galaxy, especially what happens at the Cosmic Noon.

In the past two decades, the concept of main-sequence (MS) galaxy has been established. It has been found in the majority of star-forming galaxies at any redshift that the star formation rate (SFR) and the stellar mass (M_*) are tightly correlated (e.g. [28, 29, 30]), indicating an uniformity in the star formation histories at least up to $z \approx 2$ (e.g. [31, 31, 32, 33, 34, 35]).

Great progress have been made in last decade in measuring the gas mass $M_{\rm gas}$ at high redshifts. Besides using CO(1-0) line and [CI] lines mentioned above, multiple methods such as $J > 1$ CO lines, spectral energy distribution (SED) fitting and single-band sub-millimeter/millimeter (sub-mm/mm) continuum are successfully applied, and single-ionized carbon ([CII]) is also suggested as potential molecular gas tracer for high-redshift galaxies (e.g. [36] for a recent review, and references therein). Thanks to the progress, the trend have been found that, at fixed stellar mass, the molecular gas mass of MS galaxies increases with redshift (and so does the gas fraction $f_{\rm gas} = M_{\rm gas}/(M_{\rm gas} + M_*)$) ([37]). And the higher gas fractions, attributed to more efficient gas accretion from the cosmic web at higher redshift, can explain the increase of typical SFR of MS galaxies. Such progress has also contributed to the study of the

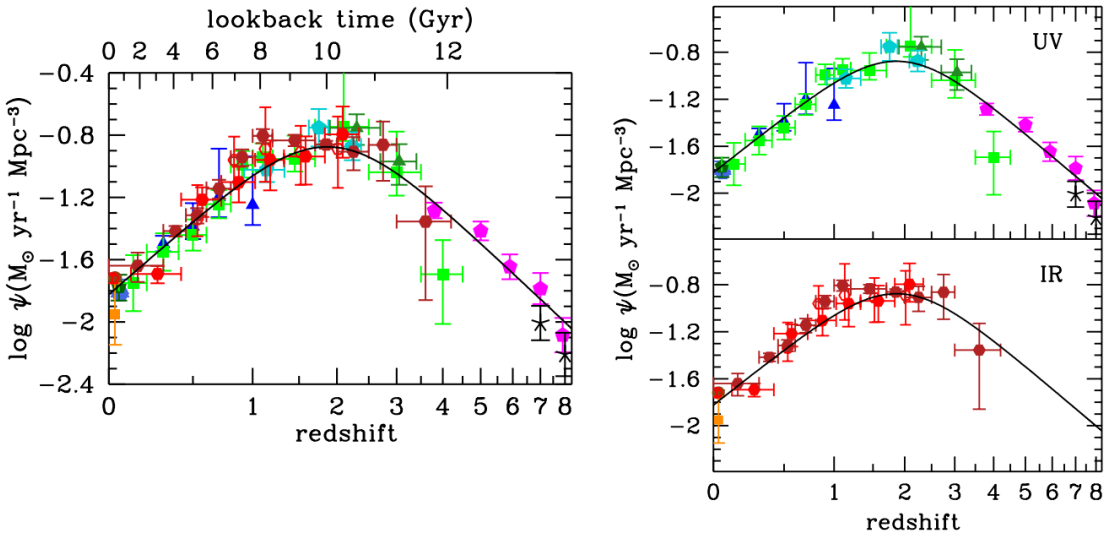

Figure 1.3: The star formation rate density as a function of redshift, from far-ultraviolet (FUV, *upper right*), infrared (IR, *lower right*) and FUV+IR (*left*). Solid lines show the best-fit SFRD across cosmic history. Figures are from [27].

evolution of star formation efficiency (SFE, defined as SFR/$M_{\rm H_2}$). It is predicted that SFE increases slowly with redshift, and early studies shows that the increase in specific SFR (sSFR, defined as SFR/M_*) of MS galaxies with redshift might be due only to the increase in gas fraction and not to the change of SFE. If so, this would imply that the peak of cosmic SFRD is caused by a larger availability of molecular gas, rather than a fundamental change in the small-scale star formation physics. However, it is also believed that a change in SFE at high redshift is also needed.

Based on above issues, a larger sample of high-redshift galaxies is needed, to help us to figure out the physics underlying the Cosmic Noon and to extend the uniformity of star-forming galaxies to higher redshift. D49 is a massive main-sequence infrared-bright galaxy, originally selected from the optically selected (*U, G, R*) sample of Lyman Break Galaxies (LBGs) in the Extended Groth Strip field (EGS) at $z \sim 3$ in [38]. Existing observations on D49 include ground-based rest-frame Ly-α emission spectroscopy, Advanced Camera for Surveys on borad Hubble Space Telescope (ACS/HST) imaging, CO(3-2) line observation with Institut de Radioastronomie Millimétrique (IRAM) Plateau de Bure Interferometer (PdBI) and multiwavelength photometric observations from optical to millimeter. In this thesis, we will add new CO(7-6), [CI](2-1) and [CI](1-0) line observations with NOEMA. These observations allow us to study D49 in extreme detail.

[39] has studied D49 based on its SED and CO(3-2) line observation. Its SED, covering from mid-IR to millimeter wavelength range, was fitted with the Draine & Li

(2007, hereafter DL07) model ([40]) to derive its infrared luminosity $L_{\rm IR}$, dust mass $M_{\rm dust}$ and dust temperature $T_{\rm dust}$. Its SFR ($600\,M_\odot\,{\rm yr}^{-1}$) and stellar mass ($M_* = 1.9\times10^{11}\,M_\odot$) were derived respectively from the infrared luminosity and the available UV to near-IR photometry with applying BC03 models assuming a constant star formation history. With the derived M_* and SFR, D49 is found to locate at the massive end of MS at $z\sim3$, shown in Figure 1.4.

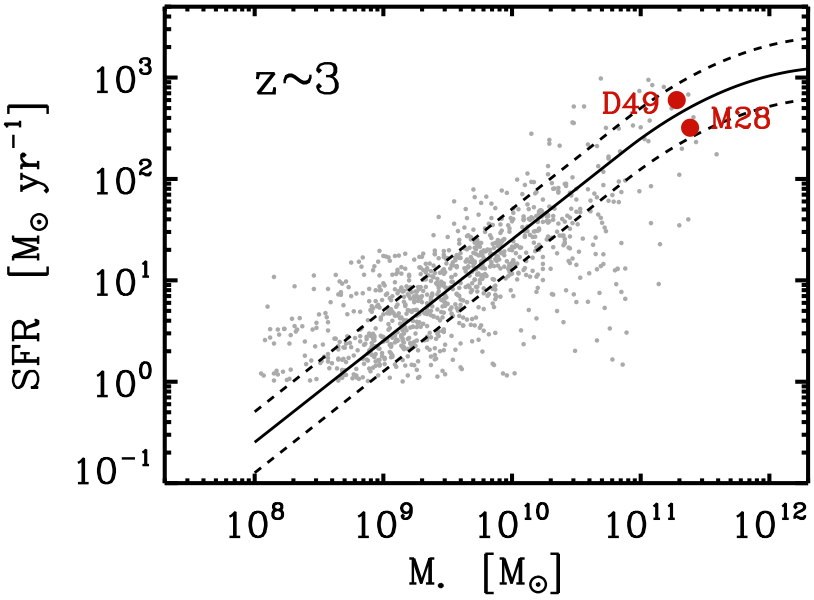

Figure 1.4: Location of D49 with respect to the main-sequence at $z\sim3$ (solid line) and its scatter (dashed line), measured by [41]. Figure is from [39].

We note that its molecular gas mass was estimated by three independent techniques:

1. **CO method**
   The molecular gas mass can be obtained from the CO(1-0) line luminosity $L'_{\rm CO}$by

$$M_{\rm H_2}[{\rm M}_\odot] = \alpha_{\rm CO}\times L'_{\rm CO}, \tag{1.5}$$

   where $\alpha_{\rm CO}$ is the CO to $M_{\rm H_2}$ conversion factor. An excitation correction $r_{31} = 0.5\pm0.15$ was adopted, based on previous studies, to convert its observed $L'_{\rm CO(3-2)}$ to $L'_{\rm CO}$. The conversion factor $\alpha_{\rm CO}$ is dependent on the metallicity of galaxy. [39] assumed a solar metallicity in D49 and used $\alpha_{\rm CO}$-Z relations in various studies to derive an average of $\alpha_{\rm CO} = 3.5$. Under these assumptions, the molecular gas mass was derived as $\log(M_{\rm H_2}[M_\odot]) = 11.48\pm0.23$.

2. **$\delta_{\rm GD}$ method**
   This method is based on the $M_{\rm gas}/M_{\rm dust}$ vs. Z relation found in local galaxies.

If we (1) know the metallicity and the $M_{\rm dust}$ of a galaxy and (2) assume the $M_{\rm gas}/M_{\rm dust}$ vs. Z relation does not vary significantly across cosmic time, we are able to derive its $M_{\rm gas}$. This method actually traces all the neutral hydrogen in the galaxy thus $M_{\rm gas} = M_{\rm H_2} + M_{\rm HI}$. But it can be assumed that $M_{\rm H_2} \gg M_{\rm HI}$, or $M_{\rm gas} \approx M_{\rm H_2}$, for the $z \sim 3$ galaxies, based on both observational and theoretical studies ([37]). Finally, the gas mass was derived as $\log(M_{\rm H_2}[M_\odot]) = 11.12 \pm 0.25$ assuming a solar metallicity in D49, and $\log(M_{\rm H_2}[M_\odot]) = 11.34 \pm 0.25$ based on metallicity derived from a broken fundamental metallicity relation (FMR, [42]), which relates the metallicity to the M_* and the SFR.

3. **Rayleigh-Jeans(R-J) method**
   This method converts the single band measurement of dust emission on the Rayleigh-Jeans side of the SED into a cold gas mass by applying the observed relation between cold dust luminosity and gas mass derived from CO(1-0) found in nearby galaxies ([43, 44]). With the calibration applied to $z \sim 3$ LBGs, the gas mass can be estimated from:

$$\begin{aligned}\log(M_{\rm H_2}[M_\odot]) = &(1.57 - 8 \times 10^{-4}\Delta\lambda) \\ &+(0.86 + 6 \times 10^{-4}\Delta\lambda)\log(\nu L_\nu[L_\odot]),\end{aligned} \tag{1.6}$$

   where $\Delta\lambda = \lambda_{\rm rest} - 250\,\mu$m and $\nu L_\nu = \nu_{\rm obs} \times S_{\nu,\rm obs} \times 4\pi \times D_{\rm L}^2$. Assuming again that $M_{\rm gas} \approx M_{\rm H_2}$, the gas mass in D49 is estimated as $\log(M_{\rm H_2}[M_\odot]) = 11.29 \pm 0.31$.

These $M_{\rm H_2}$ estimates from the various techniques are found consistent with each other within a factor of two or less, making D49 an ideal target to compare various $M_{\rm H_2}$-estimating methods.

This thesis will present the follow-up work of [39]. Combining the existing observations with our new CO and [CI] lines observations, and dust continuum measurements, we can further investigate the physical properties of molecular gas in D49 and examine how good [CI] lines serve as a tracer of gas mass. On the one hand, we focus on D49 itself and expect to figure out its properties, like gas excitation, gas mass and thus gas depletion timescale, to obtain insights on the physical driver of gas excitation and star formation activity in D49. On the other hand, from a macro perspective, D49 can serve as a template galaxy at Cosmic Noon. When compared with other main-sequence, starburst and quiescent galaxies, it may teach us how gas fractions change, how galaxies grow across cosmic time and what drives the rise of SFRD up to $z \sim 3$ and the following decline.

Throughout this thesis, the assumption that $M_{\rm gas} \approx M_{\rm H_2}$ for D49 at $z \sim 3$ is adopted, and it is also adopted that $\Omega_{\rm m} = 0.3$, $\Omega_\Lambda = 0.7$, $H_0 = 71\,{\rm km\,s^{-1}\,Mpc^{-1}}$, in addition to a Chabrier IMF ([45]).

Table 1.1: General properties of D49, measured by [39]

Name	$z_{\rm CO(3-2)}$	$\log L_{\rm IR}$ $[L_\odot]$	$\log M_*$ $[M_\odot]$	$T_{\rm dust}$ [K]	$\log L'_{\rm CO(3-2)}$ $[{\rm K\,km\,s^{-1}\,pc^2}]$
D49	2.846 ± 0.011	12.78 ± 0.03	11.28 ± 0.12	40.6 ± 2.0	10.62 ± 0.07

1.3 Thesis outline

The rest of this thesis is organized as follows: In Chapter 2, I will present the data used in this thesis, and the results of data processing and fitting, as a basis for further discussion. In Chapter 3, I will compare CO and [CI] emissions from D49 with other local and distant galaxies, and estimate the mass of gas in D49 by several methods. And finally, I will summarise this thesis in Chapter 4.

Chapter 2

Data processing and Results

2.1 Observation

D49 was observed with the NOrthern Extended Millimeter Array (NOEMA) located in France. The antennas were pointed towards (RA, Dec) = (14h:17m:29s.234, 52°:34′:34″.450). With a redshift of $z = 2.846$, the expect frequencies of CO(7-6), [CI](2-1) and [CI](1-0) are respectively 209.74 GHz, 210.43 GHz and 127.97 GHz. The CO(7-6) and [CI](2-1) lines are in the frequency range of NOEMA Band 3, while [CI](1-0) line is in the frequency range of NOEMA Band 2. For each band, the total observing time is 2.5 hours, in order to obtain a signal-noise ratio of 5 for each line.

The data were calibrated by the standard pipeline contained in the `GILDAS` package. The beam sizes are $1.93'' \times 1.48''$ (PA = 62°) and $3.19'' \times 2.50''$ (PA = 63°), respectively for Band 3 of 1.3 mm and Band 2 of 2 mm.

In the work of this thesis, I have been provided with the one-dimensional extracted spectra and the continuum, which I worked with. Therefore, the processing of raw observation data is not part of this work. The spectra were extracted with circular Gaussian profiles centered at the location of the CO(3-2) emission in [39] and with a fixed full width half maximum (FWHM) of 0.6″ (= 4.8 kpc at $z = 2.84$). The continuum emission was extracted in a similar way after averaging the line-free spectral windows. Given the spatial resolution, we did not resolve the source. This is further confirmed by the consistent continuum flux densities extracted by fitting the emission with a circular Gaussian, a point source profile, and by reading the brightest pixel in the cleaned image. Below I present the provided spectra and continuum measurements.

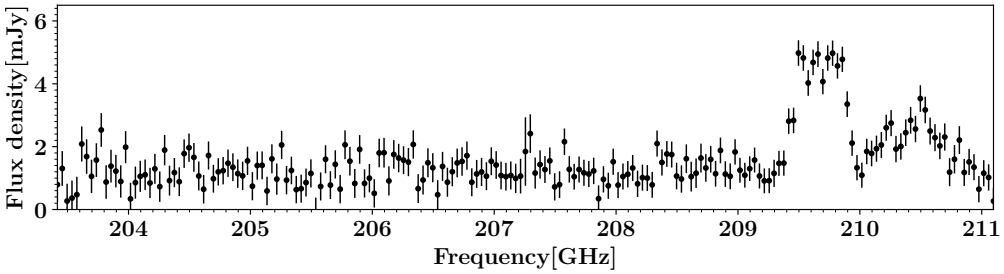

Figure 2.1: One-dimensional extracted spectrum from D49, expected to contain the emission lines CO(7-6) and [CI](2-1).

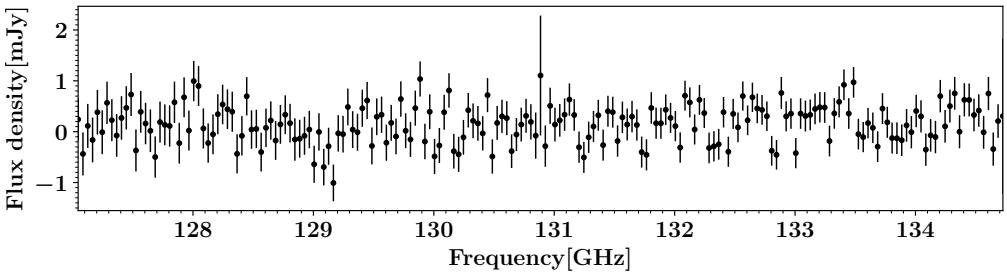

Figure 2.2: One-dimensional extracted spectrum from D49, expected to contain the emission line [CI](1-0).

Table 2.1: The continuum emission from D49.

$\lambda_{\rm obs}$ [μm]	Flux density [mJy]
1345.90	1.57 ± 0.04
2057.45	0.30 ± 0.03
2269.16	0.21 ± 0.03

2.2 CO and [CI] emission

Figure 2.1 shows the spectrum which is expected to contain CO(7-6) and [CI](2-1) emission lines. Assuming both lines can be described by Gaussian profiles and dust continuum is constant within the wavelength range of the spectrum, three models are used to fit the spectrum.

1. **"All-free" model**
   For the first model, we assume the two emission lines are independent from each other so that their central frequencies, line widths and amplitudes are independent, leading to 7 free parameters in total.

2. **"z-fixed" model**
   It is naturally that we assume two lines are in the same redshift, as they are from the same galaxy and the size of galaxy (few tens of kpc) is negligible compared to its luminosity distance ($\approx 2.3 \times 10^4$ Mpc). The observed frequencies of two lines are connected through

$$\frac{\nu_{\rm rest}^{\rm CO(7-6)}}{\nu_{\rm obs}^{\rm CO(7-6)}} = \frac{\nu_{\rm rest}^{\rm [CI](2-1)}}{\nu_{\rm obs}^{\rm [CI](2-1)}} = 1 + z. \tag{2.1}$$

3. **"z, σ-fixed" model**
   We further assume these lines trace gas that is from the same region of galaxy and thus moves in the same way. As a result, two lines share the same velocity width $\sigma_{v,\rm CO(7-6)} = \sigma_{v,\rm [CI](2-1)}$, in addition to the same redshift as assumed above.

The best-fit results are shown in Table 2.2. As the central frequency of an emission is found, we can derive its redshift and luminosity distance $D_{\rm L}$. The line width in velocity space is obtained by $\sigma_v = c \cdot \sigma / f_0$, where σ is the standard deviation of the Gaussian profile, f_0 is the frequency corresponding to a zero velocity in observation and c is the speed of light, and thus the full width at half maximum is given by FWHM $= 2.355\sigma_v$. Then the velocity integrated flux is determined by $S\Delta v = \sqrt{2\pi} \cdot F \cdot \sigma_v$, where F is the amplitude of Gaussian profile.

Figure 2.2 shows the spectrum expected to contain [CI](1-0) line. However, the [CI](1-0) line is not significant enough to be distinguished from continuum by eyes. The above three models are applied to fit [CI](1-0) line, but its redshift or (and) its line width are fixed as what we obtain from CO(7-6) and [CI](1-0) fitting. The best-fit results are shown in Table 2.3.

In Table 2.2, we find all results from three models are fully consistent within the uncertainties. The signal-to-noise ratios (SNR) of CO(7-6) line obtained from three

Table 2.2: Fitted results of CO(7-6) and [CI](2-1) from three models.

	z,σ-fixed	z-fixed	all-free	Units
Dust continuum	$(1.21 \pm 0.04) \times 10^{-3}$	$(1.21 \pm 0.04) \times 10^{-3}$	$(1.20 \pm 0.04) \times 10^{-3}$	Jy
CO(7 − 6)				
Frequency	209.69 ± 0.01	209.68 ± 0.01	209.68 ± 0.01	GHz
Redshift	2.84692 ± 0.00018	2.84700 ± 0.00020	2.84710 ± 0.00018	
$D_{\rm L}$	23532.2 ± 1.8	23533.0 ± 2.0	23534.0 ± 1.8	Mpc
Amplitude	$(3.95 \pm 0.19) \times 10^{-3}$	$(3.99 \pm 0.20) \times 10^{-3}$	$(3.98 \pm 0.20) \times 10^{-3}$	Jy
σ	0.18 ± 0.01	0.17 ± 0.01	0.18 ± 0.01	GHz
σ_v	253 ± 13	244 ± 16	252 ± 15	km/s
FWHM	595 ± 29	576 ± 37	594 ± 35	km/s
$S\Delta v$	2.50 ± 0.17	2.45 ± 0.20	2.52 ± 0.19	Jy km/s
Signal/Noise	14	12	13	
[CI](2 − 1)				
Frequency	210.39 ± 0.01	210.38 ± 0.01	210.46 ± 0.03	GHz
Redshift	2.84692 ± 0.00018	2.84700 ± 0.00020	2.84555 ± 0.00047	
$D_{\rm L}$	23532.2 ± 1.8	23533.0 ± 2.0	23518.5 ± 4.7	Mpc
Amplitude	$(1.66 \pm 0.18) \times 10^{-3}$	$(1.56 \pm 0.20) \times 10^{-3}$	$(1.69 \pm 0.20) \times 10^{-3}$	Jy
σ	0.18 ± 0.01	0.20 ± 0.03	0.19 ± 0.03	GHz
σ_v	253 ± 13	292 ± 48	277 ± 39	km/s
FWHM	595 ± 29	$(6.9 \pm 1.1) \times 10^2$	651 ± 91	km/s
$S\Delta v$	1.05 ± 0.13	1.15 ± 0.24	1.17 ± 0.21	Jy km/s
Signal/Noise	8.4	4.8	5.5	

Table 2.3: Fitted results of [CI](1-0) from three models.

	z,σ-fixed	z-fixed	all-free	Units
Dust emission	$(0.15 \pm 0.03) \times 10^{-3}$	$(0.15 \pm 0.03) \times 10^{-3}$	$(0.15 \pm 0.03) \times 10^{-3}$	Jy
[CI](1 − 0)				
Frequency	127.94	127.93	128.03 ± 5.04	GHz
Redshift	2.84692	2.84700	2.84 ± 0.15	
$D_{\rm L}$	23532	23533	23505.3 ± 1508.6	Mpc
Amplitude	$(0.27 \pm 0.20) \times 10^{-3}$	$(0.30 \pm 0.26) \times 10^{-3}$	0.004 ± 90.506	Jy
σ	0.11	0.09 ± 0.10	0.01 ± 74.94	GHz
σ_v	253	212 ± 215	25 ± 169417	km/s
FWHM	596	499 ± 507	59 ± 398977	km/s
$S\Delta v$	0.17 ± 0.13	0.16 ± 0.21	0.26 ± 5927.40	Jy km/s
Signal/Noise	1.4	0.75	4.3×10^{-5}	

models are close, while the SNR of [CI](2-1) line from z, σ-fixed model is higher than the other two. In Table 2.3, we find all-free model leads to a meaningless result, and both the other two SNRs are less than three. In terms of SNR, z, σ-fixed model is preferred. Furthermore, as our target is not spatially resolved, fixing line width allows for less free parameters in fitting and robust measurements of line ratios. Combining these facts, we adopt the z, σ-fixed result for CO(7-6) and [CI](2-1) lines, and set an upper limit for [CI](1-0) line due to its low SNR.

Following Eq.(7) in [46], the upper limit is determined as

$$S_{[\mathrm{CI}](1-0)}\Delta v < 3 \times \mathrm{RMS}_{\mathrm{channel}} \times \sqrt{6\sigma_v \mathrm{d}v}, \tag{2.2}$$

where $\mathrm{RMS}_{\mathrm{channel}}$ is the root mean square of observation errors near [CI](1-0) line, σ_v is the Gaussian width of the previous fit and $\mathrm{d}v$ is the step width of velocity channel. Here we note that the reference [CI](2-1) line with $\sigma_v \sim 250\,\mathrm{km\,s^{-1}}$ is pretty broad, which means 1-σ width is a small range compared to that of [CI](1-0), as shown in Figure 2.4 by a blue region. Thus we compute the upper limit within $\pm 3\sigma$ range, thus 6σ width in total, shown by the green region in Figure 2.4, corresponding to the $\sqrt{6}$ factor in our Eq.(2.2). The upper limit of D49 [CI](1-0) integrated flux is $0.44\,\mathrm{Jy\,km\,s^{-1}}$.

With above fitting results and upper limit, the line luminosities can be derived from Eq.(1.1). Results of three lines are summarised in Table 2.4.

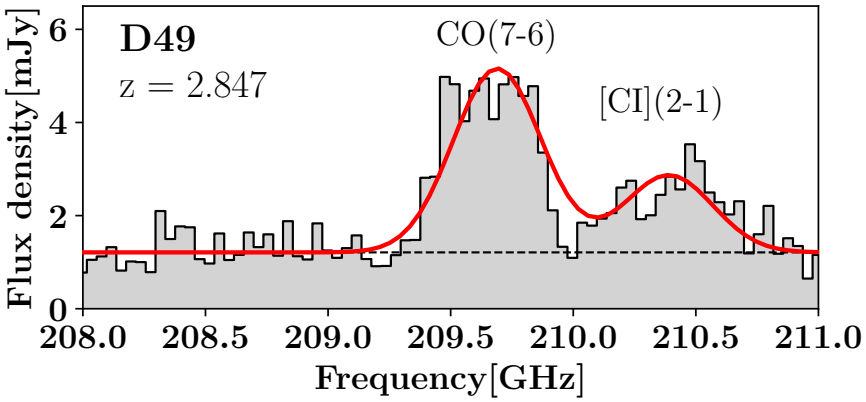

Figure 2.3: Spectrum of [CI](2-1) and CO(7-6) emissions of D49 with binned step width of $\sim 90\,\mathrm{km\,s^{-1}}$. The red curve displays the best-fitted spectral profile with fixing z and σ. The dashed line represents the constant dust continuum.

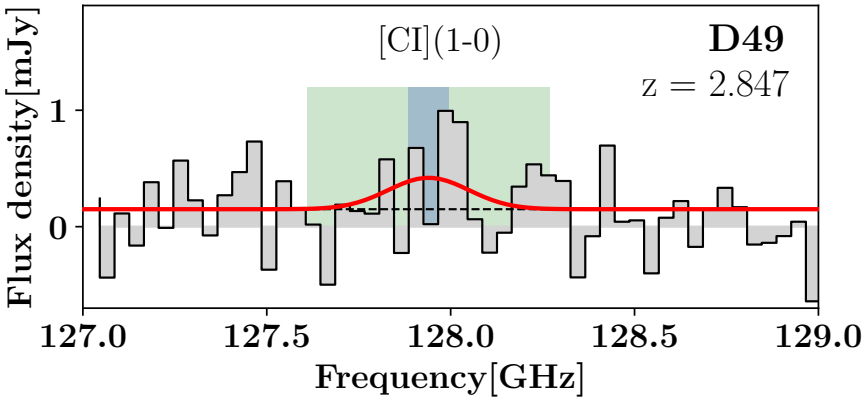

Figure 2.4: Spectrum of [CI](1-0) emissions of D49 with binned step width of $\sim 90\,\mathrm{km\,s^{-1}}$. The red curve displays the best-fitted spectral profile with fixing z and σ. The dashed line represents the constant dust continuum. The blue and green region respectively show the range of 1-σ width and 6-σ width, centered at the expected frequency on [CI](1-0) at $z = 2.847$.

Table 2.4: Best-fit results of CO and [CI] lines of D49, with setting $\sigma_{\mathrm{CO}(7-6)} = \sigma_{[\mathrm{CI}](2-1)}$ and $z_{\mathrm{CO}(7-6)} = z_{[\mathrm{CI}](2-1)}$. The upper limit on [CI](1-0) is derived from Eq.(2.2) with the best-fit redshift $z_{\mathrm{CO}(7-6)} = z_{[\mathrm{CI}](2-1)} = 2.847$.

	$S\Delta v$ [Jy km s^{-1}]	FWHM [km s^{-1}]	$\log L'$ [K km s^{-1} pc^2]
CO(7-6)	2.50 ± 0.17	595 ± 29	10.25 ± 0.03
[CI](2-1)	1.05 ± 0.13	595 ± 29	9.88 ± 0.05
[CI](1-0)	< 0.44	595	< 9.94

2.3 `Stardust` fitting

[39] have fitted mid-IR to mm spectral energy distribution(SED) of D49 with the DL07 model([47]), to derive dust mass and infrared luminosity. In this work, we extend SED to an optical-to-mm range, and fit it with a novel SED fitting algorithm, `Stardust` ([48]), which allows us to include the contribution from active galactic nuclei (AGNs).

`Stardust` can fit stellar, AGN and dust components at the same time but independently, without assuming an energy balance between the absorbed UV/optical radiation and the IR emission, as other codes assuming so (e.g. `CIGALE`, [49, 50, 51] ; `MAGPHYS`, [52, 53]). Stellar models in [54], AGN models in [55] and dust models in [40] are used in `Stardust` to create templates.

The data we use are listed in Table 2.5 and the best-fit SED is shown in Fig. 2.5. Our data includes observations from *Kitt Peak 4 m Mayall telescope* (KPNO), *Spizer telescope*, *Herschel telescope*, IRAM *30 m telescope* and NOEMA. Despite allowing for an AGN contribution in the mid-IR, the code does not provide a meaningful solution with a strong AGN ($f_{\rm AGN} = 0.01 \pm 0.33$, with SNR $\ll 3$ on the infrared luminosity contributed by AGN $L_{\rm IR}$(AGN)). In other words, the emission can be fully accounted for with stellar + dust templates. We list physical properties returned by `Stardust` fitting in Table 2.4. The infrared luminosity is consistent with what obtained in [39], but we find higher dust mass and stellar mass, and lower gas mass. The metallicity derived by FMR ([42]) and calibrated by [56] with using M_* and SFR estimates is $12 + \log({\rm O/H}) = 8.71$, which is close to the solar metallicity of ~ 8.7.

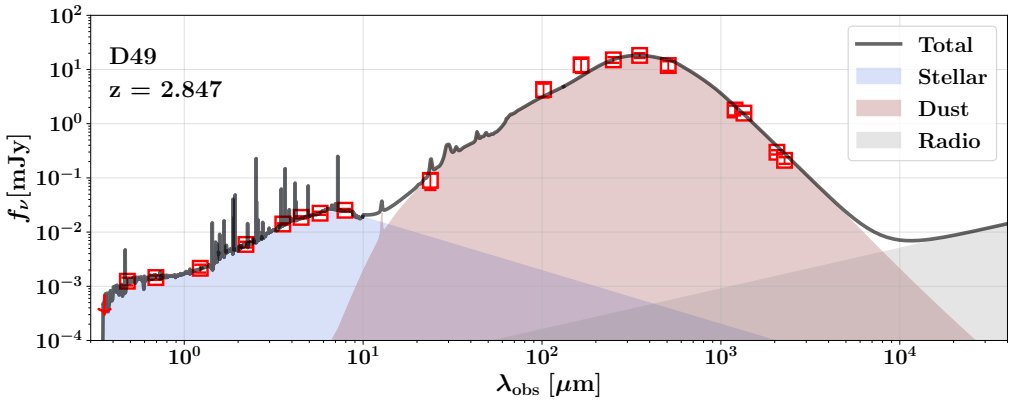

Figure 2.5: Spectral energy distribution of D49. The black line shows the `Stardust` best-fit SED, while the contribution from stars and dust are respectively shown in blue and red filled region. The grey region presents the contribution from radio continuum, based on the radio-FIR model described in [57], which is, however, not considered in `Stardust` fitting routine. It could serve as a posterior to the probability of existence of AGN ([48]).

Table 2.5: Optical to mm photometry of D49.

Band	Flux [mJy]	
KPNO, u Band[a]	1.51 ± 1.01	$\times 10^{-4}$
KPNO, g Band[a]	1.24 ± 0.21	$\times 10^{-3}$
KPNO, r Band[a]	1.45 ± 0.13	$\times 10^{-3}$
KPNO, J Band[a]	2.15 ± 0.36	$\times 10^{-3}$
KPNO, K Band[a]	5.92 ± 0.71	$\times 10^{-3}$
Spizer IRAC, 3.6 μm[a]	1.41 ± 0.04	$\times 10^{-2}$
Spizer IRAC, 4.5 μm[a]	1.87 ± 0.09	$\times 10^{-2}$
Spizer IRAC, 5.8 μm[a]	2.23 ± 0.14	$\times 10^{-2}$
Spizer IRAC, 8.0 μm[a]	2.53 ± 0.14	$\times 10^{-2}$
Spizer MIPS, 24 μm[b]	0.09 ± 0.03	
Herschel PACS, 100 μm[b]	4.27 ± 1.22	
Herschel PACS, 160 μm[b]	12.21 ± 3.56	
Herschel SPIRE, 250 μm[b]	15.08 ± 1.80	
Herschel SPIRE, 350 μm[b]	18.19 ± 1.84	
Herschel SPIRE, 500 μm[b]	11.83 ± 2.37	
IRAM 30 m Telescope, 1.2 mm[b]	1.79 ± 0.37	
NOEMA, 1.3 mm[c]	1.57 ± 0.04	
NOEMA, 2.0 mm[c]	0.30 ± 0.03	
NOEMA, 2.3 mm[c]	0.21 ± 0.03	

[a] Rigopoulou et al. (2006)
[b] Magdis et al. (2017)
[c] This work

Table 2.6: Best-fit results from `Stardust` fitting, with and without an AGN component.

	w/ AGN	w/o AGN
$\log L_{\rm IR}[L_\odot]$	12.75 ± 0.02	12.75 ± 0.02
$\log L_{\rm IR}({\rm AGN})[L_\odot]$	10.74 ± 0.56	-
$f_{\rm AGN}$	0.01 ± 0.33	-
${\rm SFR}[M_\odot\,{\rm yr}^{-1}]$	565 ± 21	566 ± 24
$\log M_{\rm dust}[M_\odot]$	9.27 ± 0.03	9.27 ± 0.03
$\log M_{\rm gas}[M_\odot]$	11.19 ± 0.03	11.19 ± 0.03
$\log M_*[M_\odot]$	11.39 ± 0.20	11.61 ± 0.16
Gas-to-dust ratio	83	83
$12 + \log({\rm O/H})$	8.71	8.71

Chapter 3

Discussions

3.1 CO and [CI] emission from D49 compared with other galaxies

In Figure 3.1, we plot relations between luminosities of three detected lines and the total infrared luminosity $L_{\rm IR}$. As a comparison, we include the local and high-redshift galaxy samples in [7] (labeled as "local" and "highz" respectively), samples in [58] (labeled as "ASPECS") and samples in [59] (labeled as "Valentino+2021"). These samples and observations were collected from different works in the literature to study how neutral atomic carbon serve as tracer across cosmic time, therefore these samples cover the range from local galaxies ($z \lesssim 0.05$) to distant galaxies ($z \sim 2-5$). The black dashed line shows linear regression between line luminosities and infrared luminosity, fitted with all the above samples with `linmix` ([60]). This code is in a Bayesian framework and fully accounts for uncertainties on both variables and upper limits on the line luminosities. The best-fit logarithmic linear regressions are

$$\log L'_{\rm CO(7-6)} = (0.93 \pm 0.02) \times \log L_{\rm IR} - (2.18 \pm 0.22),\ \sigma = 0.334 \pm 0.017, \quad (3.1)$$

$$\log L'_{\rm [CI](2-1)} = (0.83 \pm 0.02) \times \log L_{\rm IR} - (1.07 \pm 0.27),\ \sigma = 0.274 \pm 0.015, \quad (3.2)$$

$$\log L'_{\rm [CI](1-0)} = (0.75 \pm 0.03) \times \log L_{\rm IR} + (0.45 \pm 0.34),\ \sigma = 0.211 \pm 0.013, \quad (3.3)$$

where $L_{\rm IR}$ is in the unit of $L_\odot$ and line luminosities are in the unit of $\mathrm{K\,km\,s^{-1}\,pc^2}$. We find the intrinsic scatters $\sigma \lesssim 0.3\,\mathrm{dex}$ for all three correlations.

In addition, we also include two massive star-forming main-sequence galaxies BX610 ([24]) and Q1700-MD94 ([25], hereafter noted as MD94) at $z \sim 2$. Both of them are considered as typical main-sequence galaxies and have similar observation coverage as D49. Two neutral atomic carbon lines, [CI](2-1) and [CI](1-0), from these two galaxies

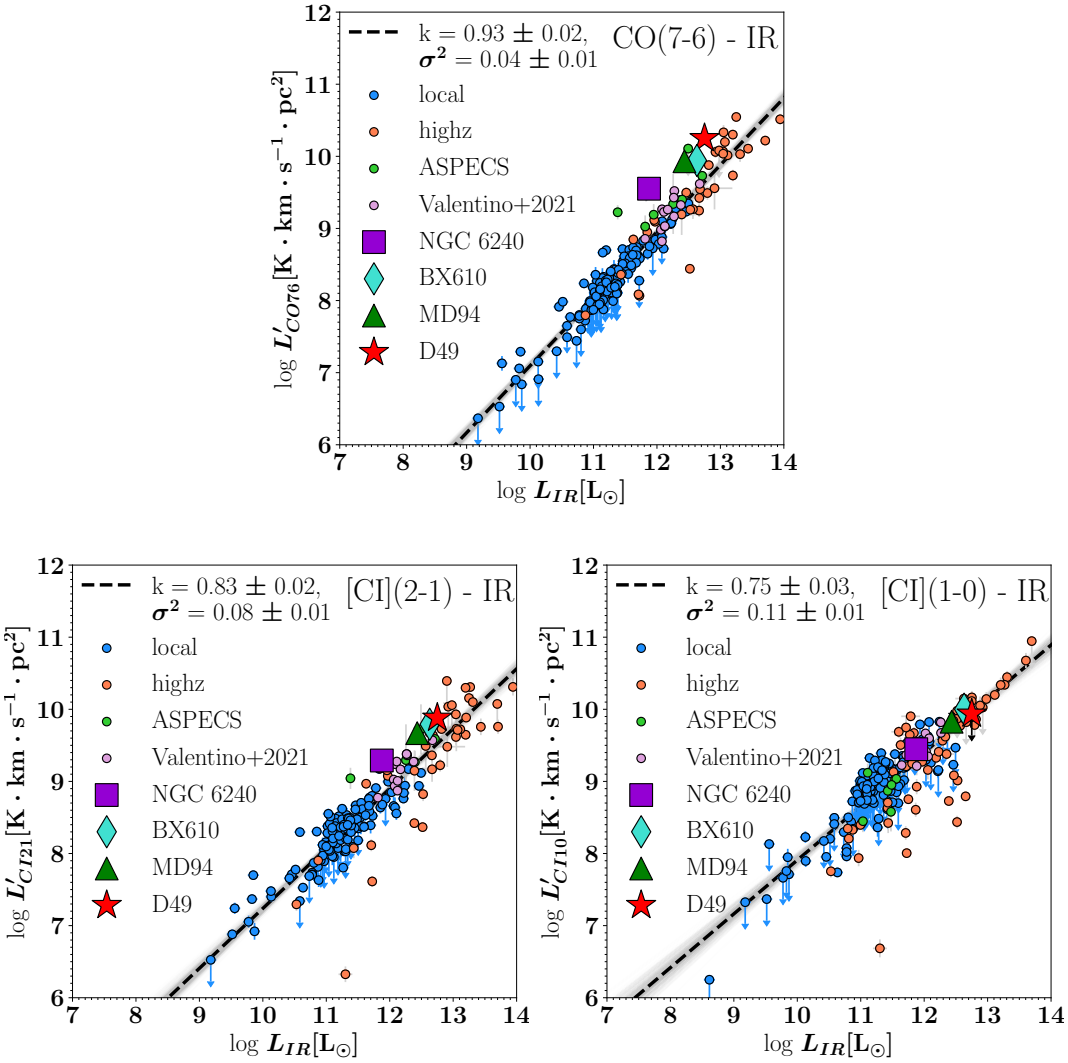

Figure 3.1: Relations between $L_{\rm IR}$ and $L'_{\rm line}$. We mark D49 as a red star, BX610 as a turquoise diamond, NGC 6240 as a purple square and MD94 as a green triangle. Blue and orange points are respectively from the local and high-redshift galaxy sample in [6], green points are the samples from [58] and pink points are from [59]. Black dashed line shows the best-fit linear correlation.

are detected, as well as several CO transitions. For MD94, its molecular gas mass estimations from dust continuum, CO emission and [CI] emission are comparable within a factor of ~ 2, suggesting [CI] a good gas mass tracer in MD94 under a set of reasonable assumptions for massive galaxies. For BX610, gas masses estimated from dust continuum and neutral carbon are consistent with each other, however both are higher than the CO-derived gas mass, which is strongly dependent on the assumption on CO conversion factor $\alpha_{\rm CO}$ of BX610. Furthermore, the mid- and high-J CO transitions are found enhanced in BX610, and the SLED analysis suggests that a shock component is needed to explain such an enhancement. A similar scenario is also found in NGC 6240, which inspires us to include it in our comparison as well.

NGC 6240 is a widely studied local galaxy (e.g. [61, 62, 63, 64]), with a triple nucleus system found in its central region ([65]). [66] found the enhanced CO emission in NGC 6240, making its CO(7-6)-to-IR ratio a outlier of local (U)LIRG samples ([67]). Its CO SLED analysis suggests a shock existing in NGC 6240 and being responsible to the CO enhancement. A high CO(7-6)-to-IR ratio is also found in D49, therefore, we compare our target D49 with NGC 6240 to find out if they are similar in some ways so that we can try to explain what may enhance the CO emission in D49, despite that NGC 6240 is a local galaxy at $z \sim 0.02$.

In Figure 3.1, we find our target galaxy D49 has a higher CO(7-6) emission than the prediction at its infrared luminosity, and so does other three galaxies NGC 6240, BX610 and MD94. As for the relation between [CI] lines and infrared luminosity, theses four galaxies follow the trend we find in our samples.

3.2 Potential shock in D49

For a Chabrier IMF ([45]), the SFR can be estimated from $L_{\rm IR}$ by ([8])

$$\mathrm{SFR}[M_\odot\,\mathrm{yr}^{-1}] = 1.0 \times 10^{-10} L_{\rm IR}[L_\odot]. \tag{3.4}$$

[67] found that CO(7-6) luminosity can also predict the SFR in local galaxies. However, NGC 6240 has a significantly higher CO(7-6)-to-IR ratio than the average ($\log \frac{L_{\rm CO(7-6)}}{L_{\rm IR}} = -4.88 \pm 0.01$). A high CO(7-6)-to-IR ratio is also reported in BX610 ([24]).

Similar to NGC 6240 and BX610, we also find a high CO(7-6)-to-IR luminosity ratio in D49. In Figure 3.2, we convert $L'_{\rm CO(7-6)}[\mathrm{K\cdot km\cdot s^{-1}\cdot pc^2}]$ to $L_{\rm CO(7-6)}[L_\odot]$ by ([8])

$$L_{\rm CO(7-6)} = 3 \times 10^{-11} \nu^3_{\rm CO(7-6)} L'_{\rm CO(7-6)}, \tag{3.5}$$

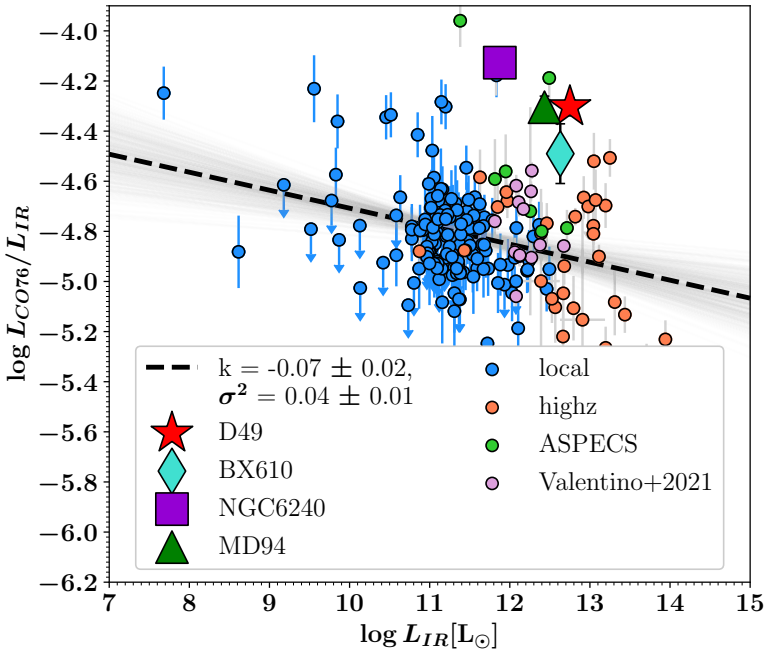

Figure 3.2: The relation of $\frac{L_{\mathrm{CO}(7-6)}}{L_{\mathrm{IR}}}$ to L_{IR}. Labels are the same as those in Figure 3.1. The best-fit correlation is re-plotted in the new coordinates, shown as dashed straight line. D49 and the other three galaxies share a high CO(7-6)-to-IR ratio, possibly enhanced by shocks.

where $\nu_{\mathrm{CO}(7-6)}$ is the rest frequency of CO(7-6) in GHz. We obtain $\log \frac{L_{\mathrm{CO}(7-6)}}{L_{\mathrm{IR}}} = -4.30 \pm 0.04$, while such a value is ~ -4.12 for NGC 6240 ([66]), and ~ -4.49 for BX610 ([24]). For MD94, we derive its $L_{IR}[L_\odot] = 10^{10} \times \mathrm{SFR}[M_\odot\,\mathrm{yr}^{-1}]$ from its SFR $= 271\,M_\odot\,\mathrm{yr}^{-1}$ ([68]) and we find a logarithmic CO(7-6)-to-IR ratio of -4.30. Following Eq.(1) in [67], the SFR of D49 derived by $L_{\mathrm{CO}(7-6)}$ would be $\sim 3500\,M_\odot$/yr, which is significantly larger than SED fitting result of $\sim 600\,M_\odot$/yr. Even though the SFR-$L_{\mathrm{CO}(7-6)}$ correlation in [67] was found in local galaxies, it is still available when applying to a high-redshift galaxy ([69]). Since the CO emission is higher than what one would expect from L_{IR} and thus SFR-driven heating mechanisms, other possibilities not affecting L_{IR} should be considered.

It is believed that the CO emissions in NGC 6240 are excited by shock ([66], [70]), and [24] suggest that shock may also exist in BX610. We therefore suspect a similar shock scenario in D49. The shock in NGC 6240 is likely caused by the collision of ISM due to merging ([66]), while the origin of shock in BX610 remains unknown. In lack of enough detected CO lines and morphological observation, we are yet unable to deduce how the shock originates and enhances CO emission in D49. Figure 3.3 presents CO spectral line energy distributions of these four galaxies, normalized by $I_{\mathrm{CO}(3-2)}$. Despite there are only two points for D49, they still show a similar trend to

those of NGC 6240 and BX610, the latter two of which can be well explained by a shock-included model. [71] determined the existence of AGN in MD94 from spectra, but its CO(7-6) is not excited as much as the other three. This implies the mechanism behind CO enhance could be more complicated than shock.

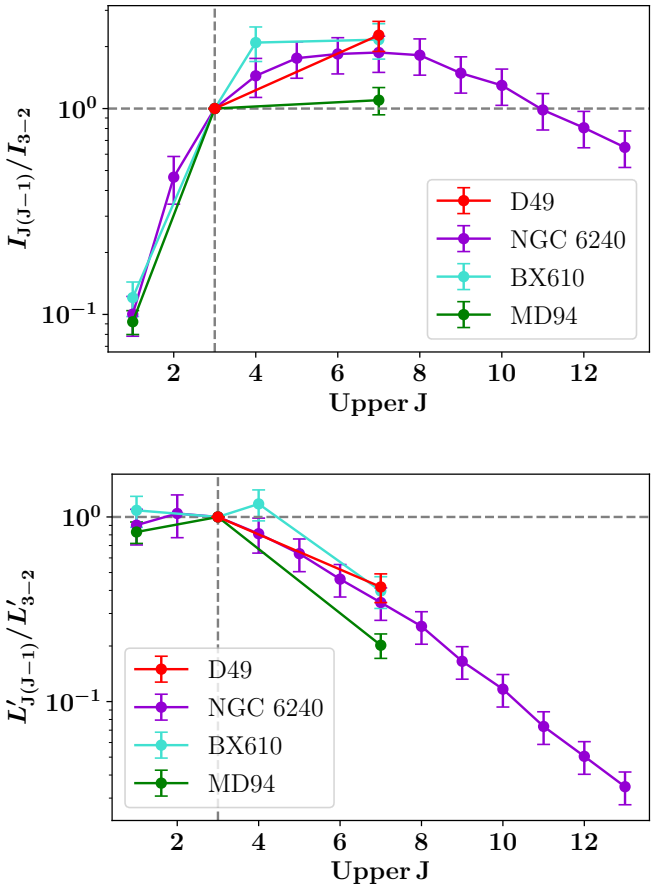

Figure 3.3: CO spectral line energy distributions of D49, compared to BX610, NGC 6240 and MD94, normalized by their own $I_{\mathrm{CO}(3-2)}$. Since a high CO(7-6)-to-IR ratio is also found in MD94, we expect MD94 an outlier in $\frac{\mathrm{CO}(3-2)}{\mathrm{IR}}$-IR relation.

3.3 [CI] as a gas mass tracer in D49

The mass of neutral carbon can be estimated from $L'_{[\mathrm{CI}](1-0)}$ by Eq.(1.4). However, with only upper limit of [CI](1-0) detected, we can only roughly estimate the lower limit of [CI] excitation temperature $T_{\mathrm{ex}} > 41\,\mathrm{K}$ and the upper limit of neutral carbon mass $M_{[\mathrm{CI}]} < 1.1\times10^7 M_\odot$. This temperature is close to the dust temperature $T_{\mathrm{dust}} = 41\pm2\mathrm{K}$ obtained by MBB model in [39].

[6] found a mean value of $\log([\mathrm{CI}]/[\mathrm{H_2}]) = -4.7 \pm 0.1$ for local MS sample at

$z \sim 1.2$, where $[\mathrm{CI}]/[\mathrm{H_2}] = M_{[\mathrm{CI}]}/(6M_{\mathrm{H_2}})$. Assuming it is also valid at $z \sim 3$, we find $M_{\mathrm{H_2}} < 9.3 \times 10^{10} M_\odot$, corresponding to $\log M_{\mathrm{H_2}} < 11.0$. Notice that the helium contribution is not included here. A factor of 1.36 should be taken into consideration to include helium, and thus the estimate is $\log M_{\mathrm{H_2}} < 11.1$. [6] also found a mean ratio of $\log(M_{[\mathrm{CI}]}/M_{\mathrm{dust}}) = -2.20 \pm 0.03$, and it leads to $M_{\mathrm{dust}} < 1.8 \times 10^9$ and thus $\log M_{\mathrm{dust}} < 9.3$. These two masses are consistent with both what we obtain from `Stardust` fitting and those in [39] within a factor of two. With the upper limit of $M_{\mathrm{H_2}}$, the gas depletion time scale will be $\tau_{\mathrm{dep}} = M_{\mathrm{H_2}}/\mathrm{SFR} < 0.22\,\mathrm{Gyr}$. This means that the galaxy will exhaust its gas mass in relatively short time and possibly transition to quiescence. This is consistent with the fact that it is a very massive objects in the bending part of the main-sequence.

We further plot logarithmic [CI](1-0)-to-IR and [CI](2-1)-to-IR ratios as functions of infrared luminosity in Figure 3.4 and Figure 3.5. Because of $L'_{[\mathrm{CI}](1-0)} \propto M_{[\mathrm{CI}]} \propto M_{\mathrm{gas}}$ and $L_{\mathrm{IR}} \propto \mathrm{SFR}$, the ratio of $L'_{[\mathrm{CI}](1-0)}$ to L_{IR} can represent the gas depletion time scale τ_{dep}. [72] found an average $\tau_{\mathrm{dep}} = 0.68^{+0.07}_{-0.08}\,\mathrm{Gyr}$ for their $z = 3.2$ sample, which means that D49 has a much shorter depletion time. Such a trend can be also found in Figure 3.4, as [CI](1-0)-to-IR ratio is lower than most of other galaxies.

In Figure 3.5, we find a tighter correlation between logarithmic [CI](1-0)-to-IR ratio and L_{IR}. According to [21], the mass of neutral carbon can be also derived from $L'_{[\mathrm{CI}](2-1)}$ as

$$M^{(2)}_{[\mathrm{CI}]} = 4.566 \times 10^{-4} Q(T_{\mathrm{ex}}) \frac{1}{5} \mathrm{e}^{62.5/T_{\mathrm{ex}}} L'_{[\mathrm{CI}](2-1)}. \tag{3.6}$$

Therefore, we obtain an upper limit of neutral carbon mass $M^{(2)}_{[\mathrm{CI}]} < 1.1 \times 10^7\,M_\odot$, which is the same as what we derive from [CI](1-0) line.

According to our measurements, we find a [CI](2-1)/[CI](1-0) line flux ratio of $\mathcal{R} = S_{[\mathrm{CI}](2-1)}\Delta v / S_{[\mathrm{CI}](1-0)}\Delta v > 2.25$. The kinetic temperature of [CI] can be derived by $T_{\mathrm{kin}} = \alpha T_{\mathrm{dust}}$ with adopting $\alpha = 1.2$ for main-sequence galaxies([73]) as $T_{\mathrm{kin}} = 49.2\,\mathrm{K}$. This temperature agrees with the previous estimation from line luminosity ratio. In Figure 3.6, we can find the molecular density of $n \approx 10^4\,\mathrm{cm^{-3}}$ and thus $Q_{10} \approx 0.45$, $Q_{21} \approx 0.3$. This allows us to estimate hydrogen mass without assuming LTE as ([74])

$$M_{\mathrm{H_2}} = 1375.8 D_{\mathrm{L}}^2 (1+z)^{-1} \left(\frac{X[CI]}{10^{-5}}\right)^{-1} \left(\frac{A_{10}}{10^{-7}\mathrm{s^{-1}}}\right)^{-1} \times Q_{10}^{-1} S_{[\mathrm{CI}](1-0)} \Delta v, \tag{3.7}$$

where $A_{10} = 10^{-7.10}\,\mathrm{s^{-1}}$ is the Einstein A coefficient. Then we obtain the estimation of hydrogen mass as $M_{\mathrm{H_2}} < 1.6 \times 10^{11}\,M_\odot$ and thus $\log M_{\mathrm{H_2}} < 11.2$. This result has

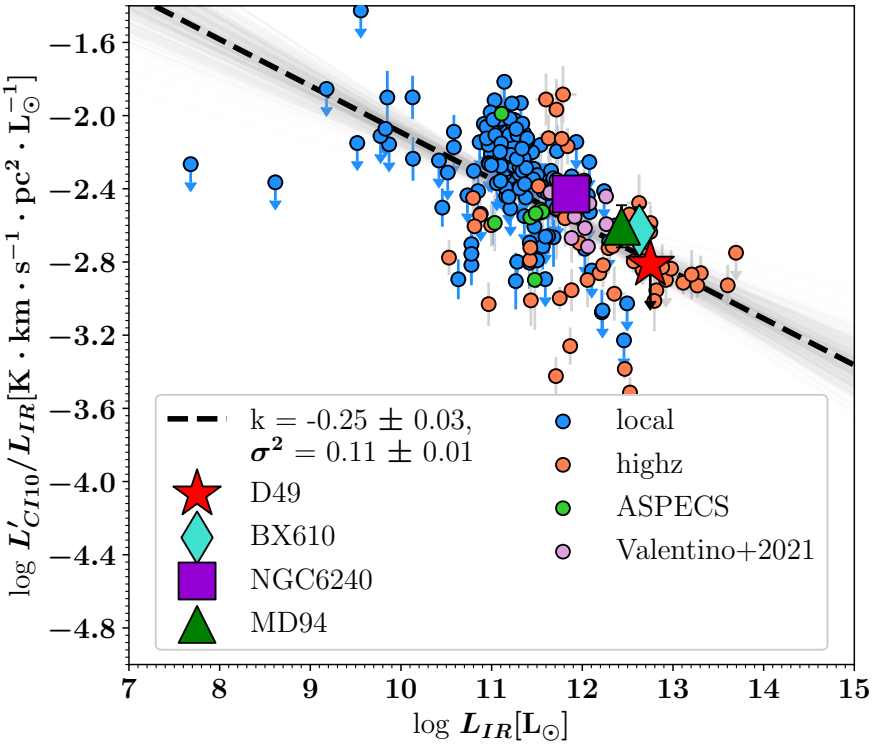

Figure 3.4: The relation of $\frac{L_{[CI](1-0)}}{L_{IR}}$ to L_{IR}. Labels are the same as those in Figure 3.1. The best-fit correlation is re-plotted in the new coordinates, shown as dashed straight line. This plot can proxy the relation between the gas depletion time scale τ_{dep} and star formation rate. Due to the upper limit of $L'_{[CI](1-0)}$, we can only derive $\tau_{dep} < 0.15\,Gyr$ for D49, which is significantly lower than what [72] found for a $z \sim 3$ sample.

included the helium contribution, and it is close to the estimation from [CI] line pair and the relative neutral carbon abundance.

Inspired by [5], the hydrogen mass can also be estimated with [CI](2-1) as

$$M_{H_2} = 1375.8 D_L^2 (1+z)^{-1} \left(\frac{X[CI]}{10^{-5}}\right)^{-1} \left(\frac{A_{21}}{10^{-7}s^{-1}}\right)^{-1} \times Q_{21}^{-1} S_{[CI](2-1)} \Delta v, \tag{3.8}$$

which leads to the same result as above.

So far, seven estimates of M_{H_2} in D49 have been derived, either from independent methods or same method but under different assumptions. The estimates are summarised in Table. 3.1. All the estimations are consistent within a factor of three or less. `Stardust` fitting gives the smallest relative error. Due to only upper limit is detected for [CI](1-0) line, we can only set upper limits when the estimations are related

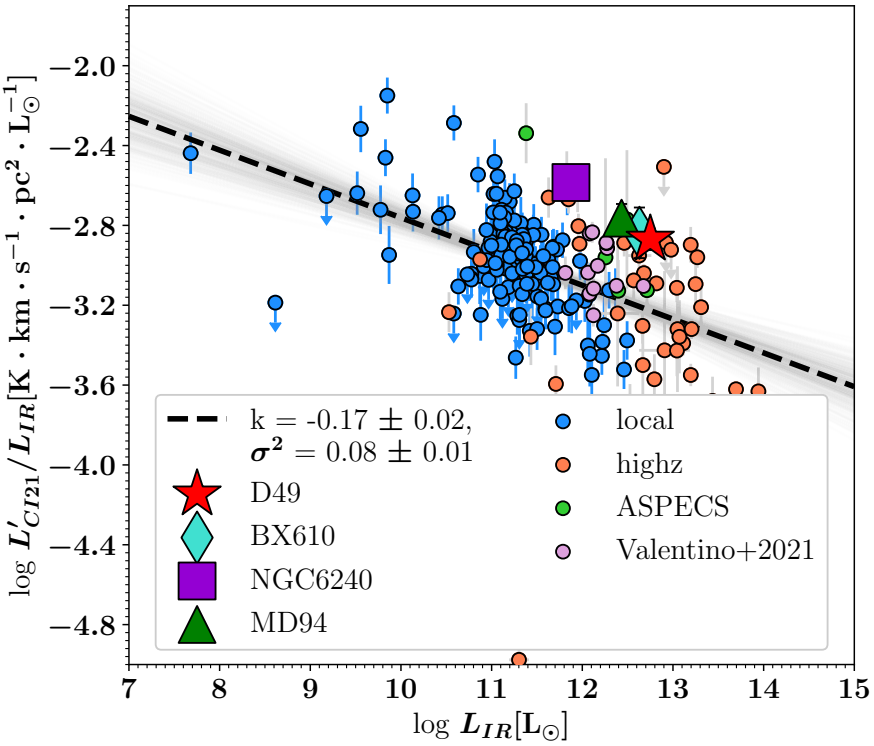

Figure 3.5: The relation of $\frac{L_{[CI](2-1)}}{L_{IR}}$ to L_{IR}. Labels are the same as those in Figure 3.1. The best-fit correlation is re-plotted in the new coordinates, shown as dashed straight line. This plot can also proxy the relation between τ_{dep} and SFR, since $[CI](2-1)$ can serve as a tracer of neutral carbon mass as well.

to [CI](1-0) line. Future observations may break this limit. We also note that those estimations from [39] are dependent on conversion factors, M_{gas}/M_{dust} vs. metallicity relation or M_{gas} dependence on R-J tail of SED, which can also cause the variation between results.

Table 3.1: Hydrogen mass estimations by different methods.

Method	Estimated $\log M_{H_2}[M_\odot]$
CO ($\langle r_{31}\rangle = 0.5 \pm 0.15$, $\alpha_{CO} = 3.5$)[a]	11.48 ± 0.23
$\delta_{GD} Z_\odot$[a]	11.12 ± 0.25
δ_{GD}"broken"FMR[a]	11.34 ± 0.25
R-J[a]	11.29 ± 0.31
`Stardust` fitting[b]	11.19 ± 0.03
[CI] pair(LTE)[b]	< 11.1
[CI] pair(non-LTE)[b]	< 11.2

[a] Magdis et al. (2017)
[b] This work

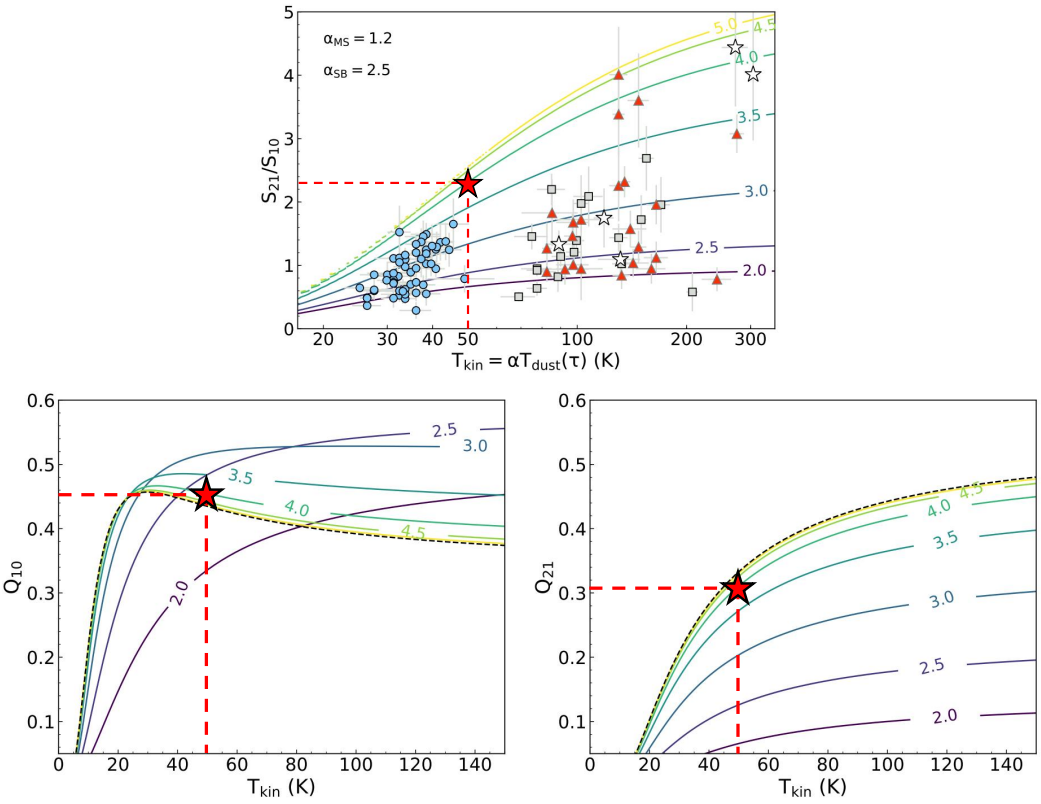

Figure 3.6: *Upper:* Neutral atomic carbon line ratio $S_{[\mathrm{CI}](2-1)}/S_{[\mathrm{CI}](1-0)}$ as a function of kinetic temperature T_{kin}. T_{kin} is connected with dust temperature T_{dust} by $T_{\mathrm{kin}} = \alpha T_{\mathrm{dust}}$, where $\alpha = 1.2$ for main-sequence galaxies and $\alpha = 2.5$ for starburst galaxies. Curves are labelled by the corresponding values of $\log(n)$, where n is the gas density. The red star shows the position of D49 in this plot, from which we find the molecular gas density $n \approx 10^4\,\mathrm{cm}^{-3}$. Figure is modified from [73]. *Lower:* The factors Q_{10} (*left*) and Q_{21} (*right*) as functions of T_{kin}, in different molecular gas density. $Q_{10} = N_1/N_{\mathrm{total}}$, where N_1 is the column density of neutral atomic carbon at its first energy level and N_{total} is the total column density of neutral atomic carbon. Q_{21} is similarly defined as $Q_{21} = N_2/N_{\mathrm{total}}$. The red stars show the positions of D49 in these two plot, from which we find $Q_{10} \approx 0.45$ and $Q_{21} \approx 0.3$ for D49. Figures are modified from [73].

Chapter 4

Conclusions

In this thesis, the properties of molecular and atomic gas in the massive main-sequence galaxy D49 at $z = 2.847$ are studied, using the new NOEMA spectra and continuum measurements. The conclusions are summarised as below:

1. Based on different physical assumption, three models are used to fit the spectra of CO(7-6), [CI](2-1) and [CI](1-0). For CO(7-6) and [CI](2-1) lines, as results from three models are consistent, the model with fixed redshift and line width is adopted due to it allows for less free parameters and robust line ratio measurement. For [CI](1-0), an upper limit is set due to its low SNR.

2. With the help of a novel SED fitting algorithm `Stardust`([48]), we fit the SED of D49 in the range of optical to millimeter. The fitting result suggests that D49 is unlikely to host a bright AGN substantially contributing to the mid- and far-IR emission.

3. We find a high logarithmic CO(7-6)-to-IR ratio of $\log \frac{L_{\mathrm{CO}(7-6)}}{L_{\mathrm{IR}}} = -4.30 \pm 0.04$. With such a ratio, the SFR predicted by CO(7-6) would be ~ 6 times larger than SFR derived from its infrared luminosity. Mechanisms enhancing CO emission but nor affecting L_{IR} should be considered. By comparing D49 with IR-bright galaxies in the local universe (NGC 6240) or objects on the main-sequence at $z \sim 2$ (BX610), we consider shocks as a possible cause of the enhanced CO(7-6) emission over the expected value based on L_{IR}. This might be due to a recent merger (similar to NGC 6240) or gas accretion, despite all gas mass estimates being consistent with the rest of MS galaxies. Future observations mapping more CO lines would help us determining the SLED at much higher accuracy and thus, via modeling, to test our hypothesis about the role of shocks in heating the molecular gas.

4. We find a lower limit of [CI] excitation temperature $T_{\rm ex} > 41\,{\rm K}$ in D49, which is close to the dust temperature $T_{\rm dust} = 41 \pm 2\,{\rm K}$ obtained by MBB model ([39]). We estimate $M_{\rm H_2}$ and $M_{\rm dust}$ with adopting the average neutral carbon abundance found in local MS sample at $z \sim 1.2$. The estimations agree with our SED fitting. We further estimate neutral carbon mass using [CI](2-1) and obtain the same result as that from [CI](1-0).

5. We apply the non-LTE assumption to our target D49 and estimate the molecular density, which allows us to estimate the $M_{\rm H_2}$. Seven estimates of $M_{\rm H_2}$ in D49 have been derived so far, either from independent methods or same method but under different assumptions. They are consistent within a factor of three or less.

Bibliography

[1] P. M. Solomon and P. A. Vanden Bout. Molecular Gas at High Redshift. *ARA&A*, 43(1):677–725, September 2005.

[2] Caitlin M. Casey, Desika Narayanan, and Asantha Cooray. Dusty star-forming galaxies at high redshift. *Phys. Rep.*, 541(2):45–161, August 2014.

[3] Alberto D. Bolatto, Mark Wolfire, and Adam K. Leroy. The CO-to-H_2 Conversion Factor. *ARA&A*, 51(1):207–268, August 2013.

[4] Padeli P. Papadopoulos and Thomas R. Greve. C I Emission in Ultraluminous Infrared Galaxies as a Molecular Gas Mass Tracer. *ApJ*, 615(1):L29–L32, November 2004.

[5] P. P. Papadopoulos, W. F. Thi, and S. Viti. CI lines as tracers of molecular gas, and their prospects at high redshifts. *MNRAS*, 351(1):147–160, June 2004.

[6] Francesco Valentino, Georgios E. Magdis, Emanuele Daddi, Daizhong Liu, Manuel Aravena, Frédéric Bournaud, Anna Cibinel, Diane Cormier, Mark E. Dickinson, Yu Gao, Shuowen Jin, Stéphanie Juneau, Jeyhan Kartaltepe, Min-Young Lee, Suzanne C. Madden, Annagrazia Puglisi, David Sanders, and John Silverman. A Survey of Atomic Carbon [C I] in High-redshift Main-sequence Galaxies. *ApJ*, 869(1):27, December 2018.

[7] Francesco Valentino, Georgios E. Magdis, Emanuele Daddi, Daizhong Liu, Manuel Aravena, Frédéric Bournaud, Isabella Cortzen, Yu Gao, Shuowen Jin, Stéphanie Juneau, Jeyhan S. Kartaltepe, Vasily Kokorev, Min-Young Lee, Suzanne C. Madden, Desika Narayanan, Gergö Popping, and Annagrazia Puglisi. The Properties of the Interstellar Medium of Galaxies across Time as Traced by the Neutral Atomic Carbon [C I]. *ApJ*, 890(1):24, February 2020.

[8] C. L. Carilli and F. Walter. Cool Gas in High-Redshift Galaxies. *ARA&A*, 51(1):105–161, August 2013.

[9] Taoling Xie, Mark Allen, and William D. Langer. Turbulent Diffusion and Its Effects on the Chemistry of Molecular Clouds. *ApJ*, 440:674, February 1995.

[10] Simon C. O. Glover, Paul C. Clark, Milica Micic, and Faviola Molina. Modelling [C I] emission from turbulent molecular clouds. *MNRAS*, 448(2):1607–1627, April 2015.

[11] H. Stoerzer, J. Stutzki, and A. Sternberg. CI fine-structure emission from non-equilibrium PDRs. *A&A*, 323:L13–L16, July 1997.

[12] J. Stutzki, F. Bensch, A. Heithausen, V. Ossenkopf, and M. Zielinsky. On the fractal structure of molecular clouds. *A&A*, 336:697–720, August 1998.

[13] P. P. Papadopoulos, W. F. Thi, and S. Viti. CI lines as tracers of molecular gas, and their prospects at high redshifts. *MNRAS*, 351(1):147–160, June 2004.

[14] Padelis P. Papadopoulos, Thomas G. Bisbas, and Zhi-Yu Zhang. New places and phases of CO-poor/C I-rich molecular gas in the Universe. *MNRAS*, 478(2):1716–1725, August 2018.

[15] Thomas G. Bisbas, Padelis P. Papadopoulos, and Serena Viti. Effective Destruction of CO by Cosmic Rays: Implications for Tracing H_2 Gas in the Universe. *ApJ*, 803(1):37, April 2015.

[16] Thomas G. Bisbas, Ewine F. van Dishoeck, Padelis P. Papadopoulos, László Szűcs, Shmuel Bialy, and Zhi-Yu Zhang. Cosmic-ray Induced Destruction of CO in Star-forming Galaxies. *ApJ*, 839(2):90, April 2017.

[17] J. Keene, D. C. Lis, T. G. Phillips, and P. Schilke. Photon dominated regions: observations of [C I] and CO. *IAU Symposium*, 178:129–139, January 1997.

[18] Roopesh Ojha, Antony A. Stark, Henry H. Hsieh, Adair P. Lane, Richard A. Chamberlin, Thomas M. Bania, Alberto D. Bolatto, James M. Jackson, and Gregory A. Wright. AST/RO Observations of Atomic Carbon near the Galactic Center. *ApJ*, 548(1):253–257, February 2001.

[19] Masafumi Ikeda, Tomoharu Oka, Ken'ichi Tatematsu, Yutaro Sekimoto, and Satoshi Yamamoto. The Distribution of Atomic Carbon in the Orion Giant Molecular Cloud 1. *ApJS*, 139(2):467–485, April 2002.

[20] S. C. Madden, D. Cormier, S. Hony, V. Lebouteiller, N. Abel, M. Galametz, I. De Looze, M. Chevance, F. L. Polles, M. Y. Lee, F. Galliano, A. Lambert-Huyghe,

D. Hu, and L. Ramambason. Tracing the total molecular gas in galaxies: [CII] and the CO-dark gas. *A&A*, 643:A141, November 2020.

[21] A. Weiß, C. Henkel, D. Downes, and F. Walter. Gas and dust in the Cloverleaf quasar at redshift 2.5. *A&A*, 409:L41–L45, October 2003.

[22] A. Weiß, D. Downes, C. Henkel, and F. Walter. Atomic carbon at redshift ∼2.5. *A&A*, 429:L25–L28, January 2005.

[23] F. Valentino, E. Daddi, A. Puglisi, G. E. Magdis, D. Liu, V. Kokorev, I. Cortzen, S. Madden, M. Aravena, C. Gómez-Guijarro, M. Y. Lee, E. Le Floc'h, Y. Gao, R. Gobat, F. Bournaud, H. Dannerbauer, S. Jin, M. E. Dickinson, J. Kartaltepe, and D. Sanders. CO emission in distant galaxies on and above the main sequence. *A&A*, 641:A155, September 2020.

[24] Drew Brisbin, Manuel Aravena, Emanuele Daddi, Helmut Dannerbauer, Roberto Decarli, Jorge González-López, Dominik Riechers, and Jeff Wagg. Neutral carbon and highly excited CO in a massive star-forming main sequence galaxy at z = 2.2. *A&A*, 628:A104, August 2019.

[25] K. Henríquez-Brocal, R. Herrera-Camus, L. Tacconi, R. Genzel, A. Bolatto, S. Bovino, R. Demarco, N. Förster Schreiber, M. Lee, D. Lutz, and M. Rubio. Molecular gas properties of Q1700-MD94: A massive main-sequence galaxy at z ≈ 2. *A&A*, 657:L15, January 2022.

[26] Andrew M. Hopkins and John F. Beacom. On the Normalization of the Cosmic Star Formation History. *ApJ*, 651(1):142–154, November 2006.

[27] Piero Madau and Mark Dickinson. Cosmic Star-Formation History. *ARA&A*, 52:415–486, August 2014.

[28] K. G. Noeske, B. J. Weiner, S. M. Faber, C. Papovich, D. C. Koo, R. S. Somerville, K. Bundy, C. J. Conselice, J. A. Newman, D. Schiminovich, E. Le Floc'h, A. L. Coil, G. H. Rieke, J. M. Lotz, J. R. Primack, P. Barmby, M. C. Cooper, M. Davis, R. S. Ellis, G. G. Fazio, P. Guhathakurta, J. Huang, S. A. Kassin, D. C. Martin, A. C. Phillips, R. M. Rich, T. A. Small, C. N. A. Willmer, and G. Wilson. Star Formation in AEGIS Field Galaxies since z=1.1: The Dominance of Gradually Declining Star Formation, and the Main Sequence of Star-forming Galaxies. *ApJ*, 660(1):L43–L46, May 2007.

[29] D. Elbaz, E. Daddi, D. Le Borgne, M. Dickinson, D. M. Alexander, R. R. Chary, J. L. Starck, W. N. Brandt, M. Kitzbichler, E. MacDonald, M. Nonino, P. Popesso,

D. Stern, and E. Vanzella. The reversal of the star formation-density relation in the distant universe. *A&A*, 468(1):33–48, June 2007.

[30] G. E. Magdis, D. Rigopoulou, J. S. Huang, and G. G. Fazio. On the stellar masses of IRAC detected Lyman Break Galaxies at z ~3. *MNRAS*, 401(3):1521–1531, January 2010.

[31] E. Daddi, D. Elbaz, F. Walter, F. Bournaud, F. Salmi, C. Carilli, H. Dannerbauer, M. Dickinson, P. Monaco, and D. Riechers. Different Star Formation Laws for Disks Versus Starbursts at Low and High Redshifts. *ApJ*, 714(1):L118–L122, May 2010.

[32] Georgios E. Magdis, E. Daddi, M. Béthermin, M. Sargent, D. Elbaz, M. Pannella, M. Dickinson, H. Dannerbauer, E. da Cunha, F. Walter, D. Rigopoulou, V. Charmandaris, H. S. Hwang, and J. Kartaltepe. The Evolving Interstellar Medium of Star-forming Galaxies since z = 2 as Probed by Their Infrared Spectral Energy Distributions. *ApJ*, 760(1):6, November 2012.

[33] M. T. Sargent, E. Daddi, M. Béthermin, H. Aussel, G. Magdis, H. S. Hwang, S. Juneau, D. Elbaz, and E. da Cunha. Regularity Underlying Complexity: A Redshift-independent Description of the Continuous Variation of Galaxy-scale Molecular Gas Properties in the Mass-star Formation Rate Plane. *ApJ*, 793(1):19, September 2014.

[34] R. Genzel, L. J. Tacconi, D. Lutz, A. Saintonge, S. Berta, B. Magnelli, F. Combes, S. García-Burillo, R. Neri, A. Bolatto, T. Contini, S. Lilly, J. Boissier, F. Boone, N. Bouché, F. Bournaud, A. Burkert, M. Carollo, L. Colina, M. C. Cooper, P. Cox, C. Feruglio, N. M. Förster Schreiber, J. Freundlich, J. Gracia-Carpio, S. Juneau, K. Kovac, M. Lippa, T. Naab, P. Salome, A. Renzini, A. Sternberg, F. Walter, B. Weiner, A. Weiss, and S. Wuyts. Combined CO and Dust Scaling Relations of Depletion Time and Molecular Gas Fractions with Cosmic Time, Specific Star-formation Rate, and Stellar Mass. *ApJ*, 800(1):20, February 2015.

[35] L. J. Tacconi, R. Genzel, A. Saintonge, F. Combes, S. García-Burillo, R. Neri, A. Bolatto, T. Contini, N. M. Förster Schreiber, S. Lilly, D. Lutz, S. Wuyts, G. Accurso, J. Boissier, F. Boone, N. Bouché, F. Bournaud, A. Burkert, M. Carollo, M. Cooper, P. Cox, C. Feruglio, J. Freundlich, R. Herrera-Camus, S. Juneau, M. Lippa, T. Naab, A. Renzini, P. Salome, A. Sternberg, K. Tadaki, H. Übler, F. Walter, B. Weiner, and A. Weiss. PHIBSS: Unified Scaling Relations of Gas Depletion Time and Molecular Gas Fractions. *ApJ*, 853(2):179, February 2018.

[36] J. A. Hodge and E. da Cunha. High-redshift star formation in the Atacama large millimetre/submillimetre array era. *Royal Society Open Science*, 7(12):200556, December 2020.

[37] Georgios E. Magdis, E. Daddi, M. Béthermin, M. Sargent, D. Elbaz, M. Pannella, M. Dickinson, H. Dannerbauer, E. da Cunha, F. Walter, D. Rigopoulou, V. Charmandaris, H. S. Hwang, and J. Kartaltepe. The Evolving Interstellar Medium of Star-forming Galaxies since z = 2 as Probed by Their Infrared Spectral Energy Distributions. *ApJ*, 760(1):6, November 2012.

[38] Charles C. Steidel, Kurt L. Adelberger, Alice E. Shapley, Max Pettini, Mark Dickinson, and Mauro Giavalisco. Lyman Break Galaxies at Redshift z ~3: Survey Description and Full Data Set. *ApJ*, 592(2):728–754, August 2003.

[39] G. E. Magdis, D. Rigopoulou, E. Daddi, M. Bethermin, C. Feruglio, M. Sargent, H. Dannerbauer, M. Dickinson, D. Elbaz, C. Gomez Guijarro, J. S. Huang, S. Toft, and F. Valentino. Dust and gas in star-forming galaxies at z 3. Extending galaxy uniformity to 11.5 billion years. *A&A*, 603:A93, July 2017.

[40] B. T. Draine and Aigen Li. Infrared Emission from Interstellar Dust. IV. The Silicate-Graphite-PAH Model in the Post-Spitzer Era. *ApJ*, 657(2):810–837, March 2007.

[41] C. Schreiber, M. Pannella, D. Elbaz, M. Béthermin, H. Inami, M. Dickinson, B. Magnelli, T. Wang, H. Aussel, E. Daddi, S. Juneau, X. Shu, M. T. Sargent, V. Buat, S. M. Faber, H. C. Ferguson, M. Giavalisco, A. M. Koekemoer, G. Magdis, G. E. Morrison, C. Papovich, P. Santini, and D. Scott. The Herschel view of the dominant mode of galaxy growth from z = 4 to the present day. *A&A*, 575:A74, March 2015.

[42] F. Mannucci, G. Cresci, R. Maiolino, A. Marconi, and A. Gnerucci. A fundamental relation between mass, star formation rate and metallicity in local and high-redshift galaxies. *MNRAS*, 408(4):2115–2127, November 2010.

[43] N. Scoville, H. Aussel, K. Sheth, K. S. Scott, D. Sanders, R. Ivison, A. Pope, P. Capak, P. Vanden Bout, S. Manohar, J. Kartaltepe, B. Robertson, and S. Lilly. The Evolution of Interstellar Medium Mass Probed by Dust Emission: ALMA Observations at z = 0.3-2. *ApJ*, 783(2):84, March 2014.

[44] N. Scoville, K. Sheth, H. Aussel, P. Vanden Bout, P. Capak, A. Bongiorno, C. M. Casey, L. Murchikova, J. Koda, J. Álvarez-Márquez, N. Lee, C. Laigle, H. J.

McCracken, O. Ilbert, A. Pope, D. Sanders, J. Chu, S. Toft, R. J. Ivison, and S. Manohar. ISM Masses and the Star formation Law at Z = 1 to 6: ALMA Observations of Dust Continuum in 145 Galaxies in the COSMOS Survey Field. *ApJ*, 820(2):83, April 2016.

[45] Gilles Chabrier. Galactic Stellar and Substellar Initial Mass Function. *PASP*, 115(809):763–795, July 2003.

[46] M. S. Bothwell, Ian Smail, S. C. Chapman, R. Genzel, R. J. Ivison, L. J. Tacconi, S. Alaghband-Zadeh, F. Bertoldi, A. W. Blain, C. M. Casey, P. Cox, T. R. Greve, D. Lutz, R. Neri, A. Omont, and A. M. Swinbank. A survey of molecular gas in luminous sub-millimetre galaxies. *MNRAS*, 429(4):3047–3067, March 2013.

[47] B. T. Draine and Aigen Li. Infrared Emission from Interstellar Dust. IV. The Silicate-Graphite-PAH Model in the Post-Spitzer Era. *ApJ*, 657(2):810–837, March 2007.

[48] Vasily I. Kokorev, Georgios E. Magdis, Iary Davidzon, Gabriel Brammer, Francesco Valentino, Emanuele Daddi, Laure Ciesla, Daizhong Liu, Shuowen Jin, Isabella Cortzen, Ivan Delvecchio, Clara Giménez-Arteaga, Carlos Gómez-Guijarro, Mark Sargent, Sune Toft, and John R. Weaver. The Evolving Interstellar Medium of Star-forming Galaxies, as Traced by Stardust. *ApJ*, 921(1):40, November 2021.

[49] D. Burgarella, V. Buat, and J. Iglesias-Páramo. Star formation and dust attenuation properties in galaxies from a statistical ultraviolet-to-far-infrared analysis. *MNRAS*, 360(4):1413–1425, July 2005.

[50] S. Noll, D. Burgarella, E. Giovannoli, V. Buat, D. Marcillac, and J. C. Muñoz-Mateos. Analysis of galaxy spectral energy distributions from far-UV to far-IR with CIGALE: studying a SINGS test sample. *A&A*, 507(3):1793–1813, December 2009.

[51] M. Boquien, D. Burgarella, Y. Roehlly, V. Buat, L. Ciesla, D. Corre, A. K. Inoue, and H. Salas. CIGALE: a python Code Investigating GALaxy Emission. *A&A*, 622:A103, February 2019.

[52] Elisabete da Cunha, Stéphane Charlot, and David Elbaz. A simple model to interpret the ultraviolet, optical and infrared emission from galaxies. *MNRAS*, 388(4):1595–1617, August 2008.

[53] A. J. Battisti, E. da Cunha, K. Grasha, M. Salvato, E. Daddi, L. Davies, S. Jin, D. Liu, E. Schinnerer, M. Vaccari, and COSMOS Collaboration. MAGPHYS+photo-z: Constraining the Physical Properties of Galaxies with Unknown Redshifts. *ApJ*, 882(1):61, September 2019.

[54] Gabriel B. Brammer, Pieter G. van Dokkum, and Paolo Coppi. EAZY: A Fast, Public Photometric Redshift Code. *ApJ*, 686(2):1503–1513, October 2008.

[55] J. R. Mullaney, D. M. Alexander, A. D. Goulding, and R. C. Hickox. Defining the intrinsic AGN infrared spectral energy distribution and measuring its contribution to the infrared output of composite galaxies. *MNRAS*, 414(2):1082–1110, June 2011.

[56] Lisa J. Kewley and Sara L. Ellison. Metallicity Calibrations and the Mass-Metallicity Relation for Star-forming Galaxies. *ApJ*, 681(2):1183–1204, July 2008.

[57] I. Delvecchio, E. Daddi, M. T. Sargent, M. J. Jarvis, D. Elbaz, S. Jin, D. Liu, I. H. Whittam, H. Algera, R. Carraro, C. D'Eugenio, J. Delhaize, B. S. Kalita, S. Leslie, D. Cs. Molnár, M. Novak, I. Prandoni, V. Smolčić, Y. Ao, M. Aravena, F. Bournaud, J. D. Collier, S. M. Randriamampandry, Z. Randriamanakoto, G. Rodighiero, J. Schober, S. V. White, and G. Zamorani. The infrared-radio correlation of star-forming galaxies is strongly $M_\star$-dependent but nearly redshift-invariant since z $\sim$ 4. *A&A*, 647:A123, March 2021.

[58] Leindert A. Boogaard, Paul van der Werf, Axel Weiss, Gergö Popping, Roberto Decarli, Fabian Walter, Manuel Aravena, Rychard Bouwens, Dominik Riechers, Jorge González-López, Ian Smail, Chris Carilli, Melanie Kaasinen, Emanuele Daddi, Pierre Cox, Tanio Díaz-Santos, Hanae Inami, Paulo C. Cortes, and Jeff Wagg. The ALMA Spectroscopic Survey in the Hubble Ultra Deep Field: CO Excitation and Atomic Carbon in Star-forming Galaxies at z = 1-3. *ApJ*, 902(2):109, October 2020.

[59] F. Valentino, E. Daddi, A. Puglisi, G. E. Magdis, V. Kokorev, D. Liu, S. C. Madden, C. Gómez-Guijarro, M. Y. Lee, I. Cortzen, C. Circosta, I. Delvecchio, J. R. Mullaney, Y. Gao, R. Gobat, M. Aravena, S. Jin, S. Fujimoto, J. D. Silverman, and H. Dannerbauer. The effect of active galactic nuclei on the cold interstellar medium in distant star-forming galaxies. *A&A*, 654:A165, October 2021.

[60] Brandon C. Kelly. Some Aspects of Measurement Error in Linear Regression of Astronomical Data. *ApJ*, 665(2):1489–1506, August 2007.

[61] S. Komossa, V. Burwitz, G. Hasinger, P. Predehl, J. S. Kaastra, and Y. Ikebe. Discovery of a Binary Active Galactic Nucleus in the Ultraluminous Infrared Galaxy NGC 6240 Using Chandra. *ApJ*, 582(1):L15–L19, January 2003.

[62] G. H. Rieke, R. M. Cutri, J. H. Black, W. F. Kailey, C. W. McAlary, M. J. Lebofsky, and R. Elston. 10 12 L starbursts and shocked molecular hydrogen in the colliding galaxies ARP 220 (=IC 4553) and NGC 6240. *ApJ*, 290:116–124, March 1985.

[63] P. Vignati, S. Molendi, G. Matt, M. Guainazzi, L. A. Antonelli, L. Bassani, W. N. Brandt, A. C. Fabian, K. Iwasawa, R. Maiolino, G. Malaguti, A. Marconi, and G. C. Perola. BeppoSAX unveils the nuclear component in NGC 6240. *A&A*, 349:L57–L60, September 1999.

[64] T. R. Greve, P. P. Papadopoulos, Y. Gao, and S. J. E. Radford. Molecular Gas in Extreme Star-Forming Environments: The Starbursts Arp 220 and NGC 6240 as Case Studies. *ApJ*, 692(2):1432–1446, February 2009.

[65] W. Kollatschny, P. M. Weilbacher, M. W. Ochmann, D. Chelouche, A. Monreal-Ibero, R. Bacon, and T. Contini. NGC 6240: A triple nucleus system in the advanced or final state of merging. *A&A*, 633:A79, January 2020.

[66] R. Meijerink, L. E. Kristensen, A. Weiß, P. P. van der Werf, F. Walter, M. Spaans, A. F. Loenen, J. Fischer, F. P. Israel, K. Isaak, P. P. Papadopoulos, S. Aalto, L. Armus, V. Charmandaris, K. M. Dasyra, T. Diaz-Santos, A. Evans, Y. Gao, E. González-Alfonso, R. Güsten, C. Henkel, C. Kramer, S. Lord, J. Martín-Pintado, D. Naylor, D. B. Sanders, H. Smith, L. Spinoglio, G. Stacey, S. Veilleux, and M. C. Wiedner. Evidence for CO Shock Excitation in NGC 6240 from Herschel SPIRE Spectroscopy. *ApJ*, 762(2):L16, January 2013.

[67] Nanyao Lu, Yinghe Zhao, C. Kevin Xu, Yu Gao, Tanio Díaz-Santos, Vassilis Charmandaris, Hanae Inami, Justin Howell, Lijie Liu, Lee Armus, Joseph M. Mazzarella, George C. Privon, Steven D. Lord, David B. Sanders, Bernhard Schulz, and Paul P. van der Werf. Measuring Star Formation Rate and Far-infrared Color in High-redshift Galaxies Using the CO(7-6) and [N II] 205 μm Lines. *ApJ*, 802(1):L11, March 2015.

[68] L. J. Tacconi, R. Neri, R. Genzel, F. Combes, A. Bolatto, M. C. Cooper, S. Wuyts, F. Bournaud, A. Burkert, J. Comerford, P. Cox, M. Davis, N. M. Förster Schreiber, S. García-Burillo, J. Gracia-Carpio, D. Lutz, T. Naab, S. Newman, A. Omont, A. Saintonge, K. Shapiro Griffin, A. Shapley, A. Sternberg,

and B. Weiner. Phibss: Molecular Gas Content and Scaling Relations in z ~1-3 Massive, Main-sequence Star-forming Galaxies. *ApJ*, 768(1):74, May 2013.

[69] Nanyao Lu, Tianwen Cao, Tanio Díaz-Santos, Yinghe Zhao, George C. Privon, Cheng Cheng, Yu Gao, C. Kevin Xu, Vassilis Charmandaris, Dimitra Rigopoulou, Paul P. van der Werf, Jiasheng Huang, Zhong Wang, Aaron S. Evans, and David B. Sanders. CO (7-6), [C I] 370 μm, and [N II] 205 μm Line Emission of the QSO BRI 1335-0417 at Redshift 4.407. *ApJ*, 864(1):38, September 2018.

[70] N. Lu, Y. Zhao, C. K. Xu, Y. Gao, L. Armus, J. M. Mazzarella, K. G. Isaak, A. O. Petric, V. Charmandaris, T. Díaz-Santos, A. S. Evans, J. Howell, P. Appleton, H. Inami, K. Iwasawa, J. Leech, S. Lord, D. B. Sanders, B. Schulz, J. Surace, and P. P. van der Werf. Warm Molecular Gas in Luminous Infrared Galaxies. *ApJ*, 787(2):L23, June 2014.

[71] Dawn K. Erb, Charles C. Steidel, Alice E. Shapley, Max Pettini, Naveen A. Reddy, and Kurt L. Adelberger. Hα Observations of a Large Sample of Galaxies at z ~2: Implications for Star Formation in High-Redshift Galaxies. *ApJ*, 647(1):128–139, August 2006.

[72] E. Schinnerer, B. Groves, M. T. Sargent, A. Karim, P. A. Oesch, B. Magnelli, O. LeFevre, L. Tasca, F. Civano, P. Cassata, and V. Smolčić. Gas Fraction and Depletion Time of Massive Star-forming Galaxies at z ~3.2: No Change in Global Star Formation Process out to z > 3. *ApJ*, 833(1):112, December 2016.

[73] P. Papadopoulos, L. Dunne, and S. Maddox. The subthermal excitation of the C I lines in the molecular gas reservoirs of galaxies: its significance and potential utility. *MNRAS*, 510(1):725–733, February 2022.

[74] M. S. Bothwell, J. E. Aguirre, M. Aravena, M. Bethermin, T. G. Bisbas, S. C. Chapman, C. De Breuck, A. H. Gonzalez, T. R. Greve, Y. Hezaveh, J. Ma, M. Malkan, D. P. Marrone, E. J. Murphy, J. S. Spilker, M. Strandet, J. D. Vieira, and A. Weiß. ALMA observations of atomic carbon in z $\sim$ 4 dusty star-forming galaxies. *MNRAS*, 466(3):2825–2841, April 2017.